RSC Advances

PAPER

View Article Online
View Journal | View Issue

Cite this: *RSC Adv.*, 2023, **13**, 26822

Iron/vanadium co-doped tungsten oxide nanostructures anchored on graphitic carbon nitride sheets (FeV-WO_3@g-C_3N_4) as a cost-effective novel electrode material for advanced supercapacitor applications

Sajida Parveen,[a] Eric W. Cochran,[b] Sonia Zulfiqar,[bc] Mohammed A. Amin,[d] Muhammad Farooq Warsi *[a] and Khadija Chaudhary*[a]

In this work, we studied the effect of iron (Fe) and vanadium (V) co-doping (Fe/V), and graphitic carbon nitride (g-C_3N_4) on the performance of tungsten oxide (WO_3) based electrodes for supercapacitor applications. The lone pair of electrons on nitrogen can improve the surface polarity of the g-C_3N_4 electrode material, which may results in multiple binding sites on the surface of electrode for interaction with electrolyte ions. As electrolyte ions interact with g-C_3N_4, they quickly become entangled with FeV-WO_3 nanostructures, and the contact between the electrolyte and the working electrode is strengthened. Herein, FeV-WO_3@g-C_3N_4 is fabricated by a wet chemical approach along with pure WO_3 and FeV-WO_3. All of the prepared samples *i.e.*, WO_3, FeV-WO_3, and FeV-WO_3@g-C_3N_4 were characterized by XRD, FTIR, EDS, FESEM, XPS, Raman, and BET techniques. Electrochemical performance is evaluated by cyclic voltammetry (CV), galvanic charge/discharge (GCD), and electrochemical impedance spectroscopy (EIS). It is concluded from electrochemical studies that FeV-WO_3@g-C_3N_4 exhibits the highest electrochemical performance with specific capacitance of 1033.68 F g^{-1} at scan rate 5 mV s^{-1} in the potential window range from −0.8 to 0.25 V, that is greater than that for WO_3 (422.76 F g^{-1}) and FeV-WO_3 (669.76 F g^{-1}). FeV-WO_3@g-C_3N_4 has the highest discharge time (867 s) that shows it has greater storage capacity, and its coulombic efficiency is 96.7%, which is greater than that for WO_3 (80.1%) and FeV-WO_3 (92.1%), respectively. Furthermore, excellent stability up to 2000 cycles is observed in FeV-WO_3@g-C_3N_4. It is revealed from EIS measurements that equivalent series resistance and charge transfer values calculated for FeV-WO_3@g-C_3N_4 are 1.82 Ω and 0.65 Ω, respectively.

Received 18th June 2023
Accepted 14th August 2023

DOI: 10.1039/d3ra04108e

rsc.li/rsc-advances

1. Introduction

The indiscriminative use of non-renewable resources of energy such as coal, oil, and natural gas, *etc.* for the generation of power causes environmental issues like climate change and depletion of fossil fuels. Furthermore, the planet's population is expanding quickly, and also their social desire to speed up the energy-generation and storage processes even more.[1,2] In view of this scenario, extensive work is being done on environment friendly and renewable technologies for energy storage to limit the use of traditional energy resources and reduce environmental pollution.[3–5] Different energy storage technologies, such as lithium-ion batteries (LIBs), capacitors, supercapacitors, and other energy storage devices are commonly available to fulfill market requirements. LIBs are excellent electrochemical devices because of their large energy density,[6] however, they have low energy output and short lifespan because of the thick and heavy electrodes, and poor electron transfer.[7]

Supercapacitors as energy storage devices are classified into different categories, as electrical double layer capacitors (EDLCs), pseudo-capacitors, and hybrid capacitors. Pseudo-capacitors have higher capacitance values than EDLCs. Supercapacitors with efficient power density and higher sustainability are highly recommended for electric and hybrid vehicles as well as for electronics and backup energy systems.[8–10] Although supercapacitors are ideal for purposes that need relatively efficient improvements of power, such as power supply in exigent circumstances and peak power output that assists batteries in electric and hybrid vehicles, the energy storage characteristics

[a]*Institute of Chemistry, Baghdad-ul-Jadeed Campus, The Islamia University of Bahawalpur, Bahawalpur 63100, Pakistan. E-mail: farooq.warsi@iub.edu.pk; khadija.chaudhary.kc@gmail.com*

[b]*Department of Chemical and Biological Engineering, Iowa State University, Sweeney Hall, 618 Bissell Road, Ames, Iowa 50011, USA*

[c]*Department of Chemistry, Faculty of Science, University of Ostrava, 30. Dubna 22, Ostrava 701 03, Czech Republic*

[d]*Department of Chemistry, College of Science, Taif University, PO Box 11099, Taif 21944, Saudi Arabia*

of supercapacitors still need improvement.[11] Many of the transition metal oxides have been used as electrode material for supercapacitors, such as MoO_3,[12] ZnO,[13] MnO_2,[14] NiO,[15] Co_3O_4,[16] V_2O_5,[17] CuO,[18] NiS,[19] and CoS[20] due to pseudo-capacitive behavior. These days, the majority of researchers in this field are working on improving the electrode durability and specific capacitance. The nature of the electrode material determines a supercapacitor's entire electrochemical behavior and the electrodes with organized morphology are capable of achieving high capacitance value.[21–26]

Supercapacitors based on WO_3 have been thoroughly explored and frequently reported.[27–29] WO_3 demonstrates pseudo-capacitive behavior due to its various oxidation states, quick surface interactions, and favorable crystalline structure for the interactions with electrolyte ions. It has lately gained attention as a potential electrode material in the fabrication of pseudo-capacitors due to its outstanding capacitive performance and natural availability.[30–33] Additionally, WO_3 is known to be a potential contender for electro-catalytic performance,[34] in gas sensors,[35] electro-chromism,[36] rechargeable LIBs,[37] dye sensitized solar cells,[38] and for energy storage. The prime choice for supercapacitors is that the active material should have high electrical conductance and be capable of providing excellent electrical performance. Hence, multiple attempts have been made to improve WO_3 efficiency.

Several researchers have worked on different strategies to improve the properties of WO_3. WO_3 has been doped with various types of metals to enhance its efficiency as a photoactive material in photoelectrochemical water splitting mechanism.[39–43] Further, the energy storage characteristics of WO_3 can also be improved by doping with different transition metal elements. For instance, Gupta *et al.* used a hydrothermal technique to synthesize Pd@WO_3 nanostructures with enhanced energy density for energy storage applications.[44] Kumar *et al.* manufactured Ni@WO_3 and $NiWO_4$ nanostructures by a microwave method for supercapacitor applications.[45] VWO_3 electrodes have drawn more interest.[46–49] In general, it has been demonstrated that increasing the energy and power density of W containing cathode layers through the doping of ecologically favorable and sustainable V elements is an effective strategy.[49] Further, compositing WO_3 with other metal oxides or carbon supports is another strategy to improve its performance. The selection of components for the manufacturing of composite depends on how efficiently they work together. In comparison to metal oxides, carbon materials usually have high conductivity, specific energy, and surface area. Therefore, active material can be deposited on highly conductive materials such as CNTs, graphene, and graphitic carbon nitride (g-C_3N_4) to increase the electrical conductivity of the bare samples. The nitrogen element of g-C_3N_4 renders it suitable for supercapacitor and battery uses.[50] The lone pair of electrons on nitrogen improves the surface polarity of g-C_3N_4 based electrode material, resulting in multiple binding sites on the electrode surface, which in turn enhances the wettability and affinity of electrode material for electrolyte ions. In addition, enhancement in surface area after the addition of carbon-based g-C_3N_4 helps in better dispersion of active sites or improves the electroactive surface area for charge storage. Metal oxides with a pseudo-capacitive nature can be effectively integrated with g-C_3N_4 structure in order to enhance the electrochemical performance of the subsequent electrode material.[50–54]

Hence, in this work, we first time report the influence of Fe and V co-doping and g-C_3N_4 fabrication on the structural, functional, morphological, and electrochemical performance of the WO_3 for supercapacitor study. WO_3 and FeV-WO_3 were synthesized by co-precipitation method and its composite with (g-C_3N_4) was successfully fabricated by ultra-sonication technique. The electrochemical efficiency of FeV-WO_3@g-C_3N_4 was compared with pure WO_3 and FeV-WO_3, and prepared samples were analyzed by different characterization techniques *i.e.* XRD, FTIR, FESEM, EDS, XPS, Raman, and BET analysis. The electrochemical measurements were also carried out by CV, GCD, and EIS measurements.

2. Experimental part

2.1. Materials

Sodium tungstate (Na_2WO_4), ethylene glycol ($C_2H_6O_2$), hydrochloric acid (HCl), ammonium metavanadate (NH_4VO_3), iron(III) nitrate ($Fe(NO_3)_3$), sodium sulfate (Na_2SO_4), sodium carboxy methyl cellulose (SCMC), and ethanol (C_2H_6O) were used. The chemicals were pure and used without further purification.

2.2. Synthesis of FeV-WO_3

Iron vanadium co-doped tungsten oxide (FeV-WO_3) was prepared by adding 0.2 g of ammonium metavanadate (NH_4VO_3), 0.2 g of iron nitrate ($Fe(NO_3)_3$), and 2 g of sodium tungstate (Na_2WO_4) into the mixture of water and ethylene glycol (volumetric ratio of 1 : 2). Obtained solution was stirred at 75 °C for almost 10 min along with continuous addition of 10 mL conc. HCl until pH $\sim$ 2 was achieved. After that, reaction was allowed to age for 12 h. Precipitates were washed with distilled water and ethanol successively until it became neutral. Then, the brown green colored FeV-WO_3 precipitates were dried in the electric oven at 85 °C. Next, dried precipitates were annealed at 250 °C for 3 h and ground well to fine powder. In addition, pure WO_3 was also synthesized for comparison following the same methodology without adding NH_4VO_3 and Fe $(NO_3)_3$ during the first step.

2.3. Synthesis of graphitic carbon nitride (g-C_3N_4)

Appropriate amount of melamine was taken in a ceramic crucible and placed in the lab furnace for annealing at 500 °C for 2 h. The yellow-colored powder obtained was allowed to cool down and then ground in to fine powder. For exfoliation, as obtained powdered material was added in water and ultrasonicated for 5 h and then dried in the electric oven. Hence, graphitic carbon nitride (g-C_3N_4) was obtained. It was used for the synthesis of the composite.

2.4. Synthesis of FeV-WO_3@g-C_3N_4

The composite of FeV-WO_3 was prepared with g-C_3N_4 through ultra-sonication method. Briefly, FeV-WO_3 and g-C_3N_4 were

taken in 8 : 2 ratio in 20 mL distilled water. After ultrasonication of the solution for 2 h, the homogeneous suspension was dried in the electric oven at 60 °C. Finally, brown yellow colored powder of FeV-WO_3@g-C_3N_4 was obtained.

2.5. Electrochemical tests

All the electrochemical measurements *i.e.*, GCD, CV, and EIS were performed with the GAMRY interface/5000E consisting of three electrodes with 1 M Na_2SO_4 as an electrolyte. Platinum wire and Ag/AgCl were utilized as counter and reference electrodes. For working electrode, 0.005 g of the prepared samples were added into 3 μL of sodium carboxy methyl cellulose (SCMC) and then 1 mL of ethanol was added into it. Nickel foam was cut into a piece of 2 cm in length and 1 cm in width, washed with HCl, and dried in oven at 60 °C. The mixture for working electrode was loaded on Ni foam and dried at 60 °C. The whole synthesis process and fabrication of electrode are schematically shown in Fig. 1.

3. Results and discussion

3.1. Phase analysis

The structural analysis of as fabricated samples *i.e.*, WO_3, FeV-WO_3, and FeV-WO_3@g-C_3N_4 was performed by X-ray diffraction technique, as shown in Fig. 2(a). XRD pattern of WO_3 showed peaks at 2θ values of 23.13°, 24.05°, 28.91°, 33.83°, 42.02°, 45.41°, 47.37°, 49.45°, 50.76°, 55.03°, 60.05°, 61.25°, 63.10°, 69.77°, 71.51°, 74.113°, and 76.75°, which can be assigned to (101), (201), (111), (300), (211), (002), (220), (310), (112), (221), (400), (212), (401), (222), (312), (103), and (330) diffraction planes, respectively (JCPDS# 33-1387). It confirms the monoclinic crystal phase of WO_3. High intensity of peaks showed the excellent crystalline nature of WO_3.[55] XRD pattern of FeV-WO_3 is almost identical to the WO_3, although there is slight peak shifting to higher 2θ values which may result from the contraction in lattice parameters after the doping of Fe and V ions in parent lattice of WO_3 (Fig. 2(b)). In XRD pattern of FeV-WO_3@g-C_3N_4, an additional peak appeared at 27.2° in correspondence to (002) plane which is the distinguishable peak of g-C_3N_4.[56] It is noteworthy that the diffraction peaks of FeV-WO_3@g-C_3N_4 shifted to a lower angle as compared to FeV-WO_3, with increase in the breadth of peaks (indicated by peak corresponding to (300) plane in Fig. 2(b)). This peak shifting of (300) plane can be explained in terms of changes in *d*-spacing and other crystallite parameters as a result of inclusion of g-C_3N_4 sheets in FeV-WO_3@g-C_3N_4 composite.[57,58] Appearance of (002) plane and peak shifting confirms the successful assembly of FeV-WO_3 with g-C_3N_4 sheets.

3.2. Functional group analysis

For the functional group analysis of all the prepared samples, FTIR technique was used. FTIR spectra of all the three prepared samples *i.e.*, WO_3, FeV-WO_3, and FeV-WO_3@g-C_3N_4 are exhibited in Fig. 3(a)–(c) in the wavenumber range of 500–4000 cm^{-1}. FTIR spectrum of the WO_3 show a broad band in the range of 500 cm^{-1} to 1000 cm^{-1}. In Fig. 3(a), bands in the spectrum of WO_3 at 644 cm^{-1} and 925 cm^{-1} clearly indicate the O–W–O vibrations and band that appeared at 3446 cm^{-1} is assigned to the stretching mode of the O–H group due to the adsorbed water.[59,60] Similarly, in FTIR spectrum of FeV-WO_3 two bands appeared at 650 cm^{-1} and 925 cm^{-1} show O–W–O vibrational modes (Fig. 3(b)).[61] The band at 3626 cm^{-1} is due to the stretching vibration of O–H.[62] In the FTIR spectrum of FeV-WO_3@g-C_3N_4, various bands are shown

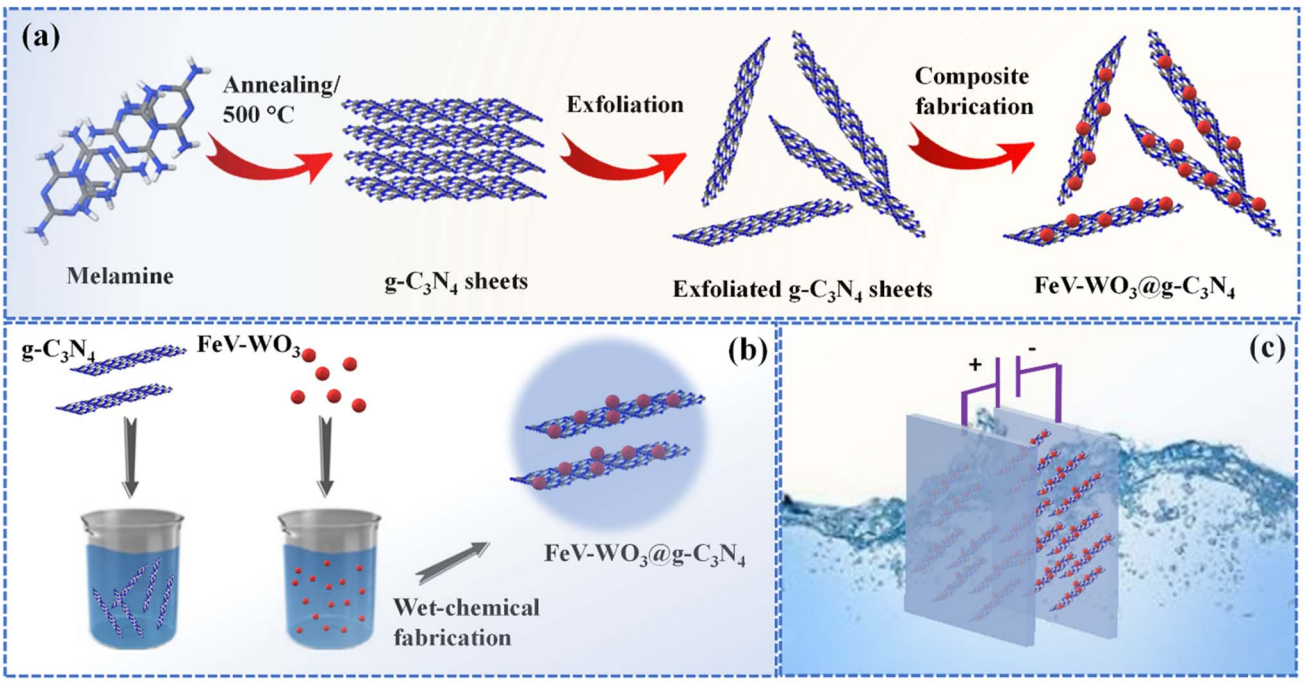

Fig. 1 Schematic representation of (a and b) synthesis of FeV-WO_3@g-C_3N_4 composite and (c) fabrication of electrode.

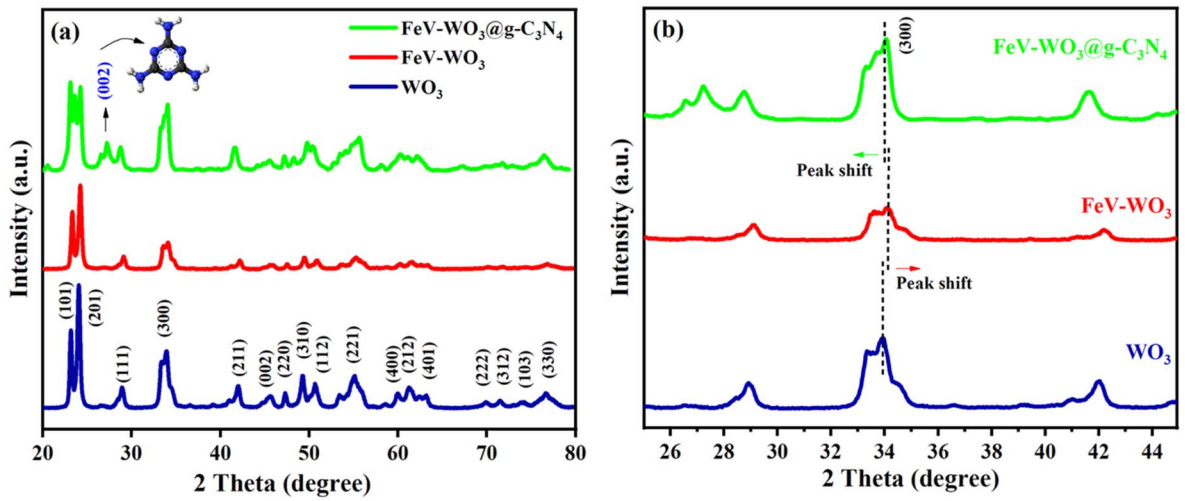

Fig. 2 (a) XRD patterns of prepared WO_3, FeV-WO_3, and FeV-WO_3@g-C_3N_4 composite, and (b) peak shift in XRD peaks of WO_3, FeV-WO_3, and FeV-WO_3@g-C_3N_4 composite.

in the region of 500–1632 cm^{-1} (Fig. 3(c)).[63] Bands that appeared at 631 cm^{-1}, and 937 cm^{-1} indicate the O–W–O vibrational modes. The bands at 1237 cm^{-1}, 1320 cm^{-1}, and 1421 cm^{-1} demonstrate different vibrational modes from g-C_3N_4 ring. The band that emerged at 3620 cm^{-1} is attributed to O–H stretching vibration.[64]

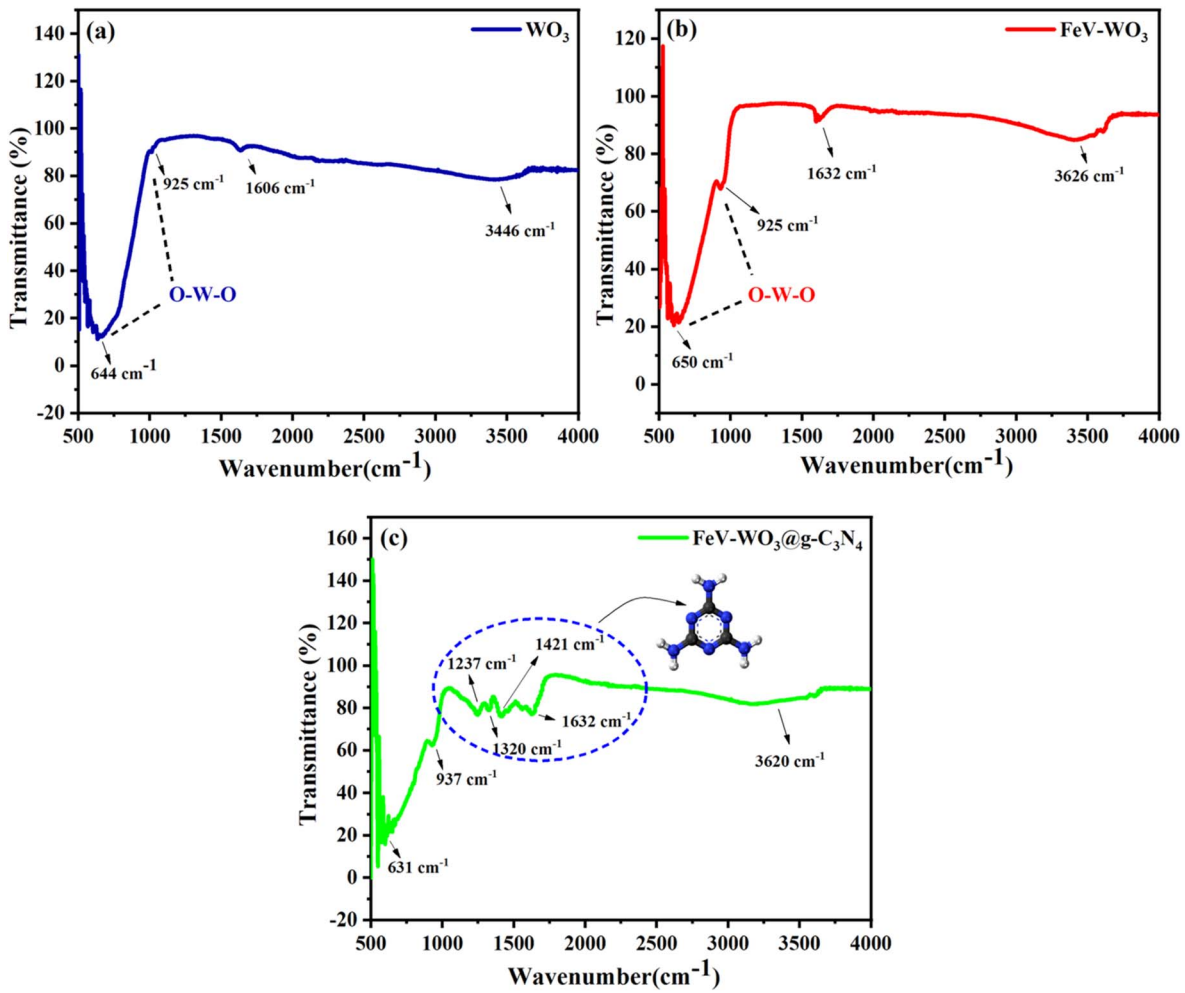

Fig. 3 FTIR spectra of (a) WO_3, (b) FeV-WO_3, and (c) FeV-WO_3@g-C_3N_4 composite.

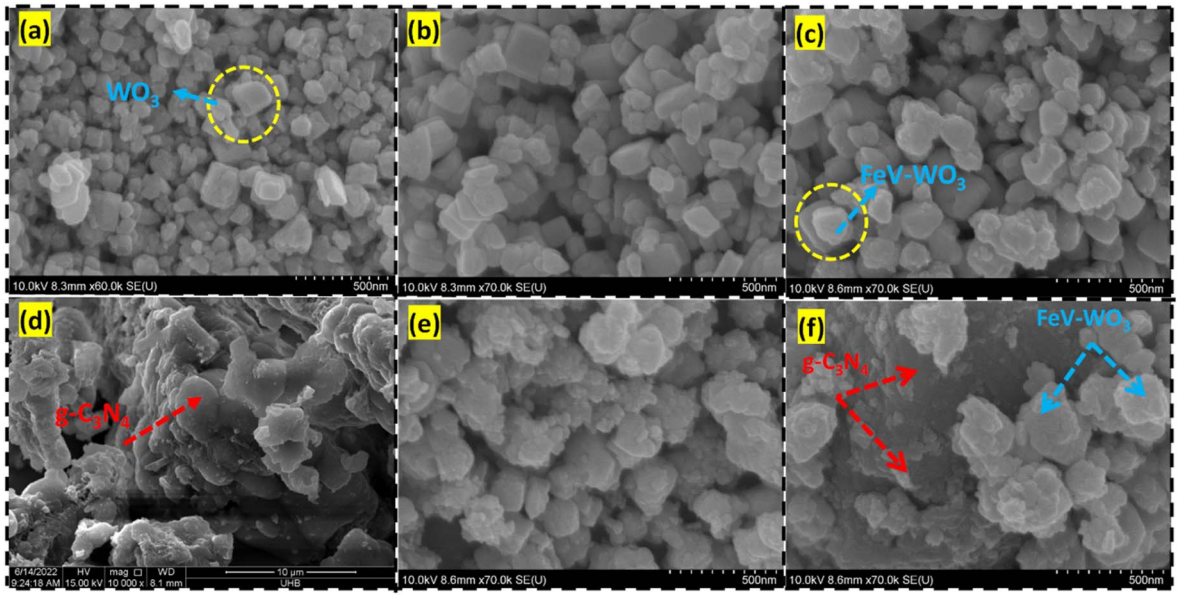

Fig. 4 FESEM images of (a and b) WO_3, (c) FeV-WO_3, (d) g-C_3N_4, and (e and f) FeV-WO_3@g-C_3N_4 composite.

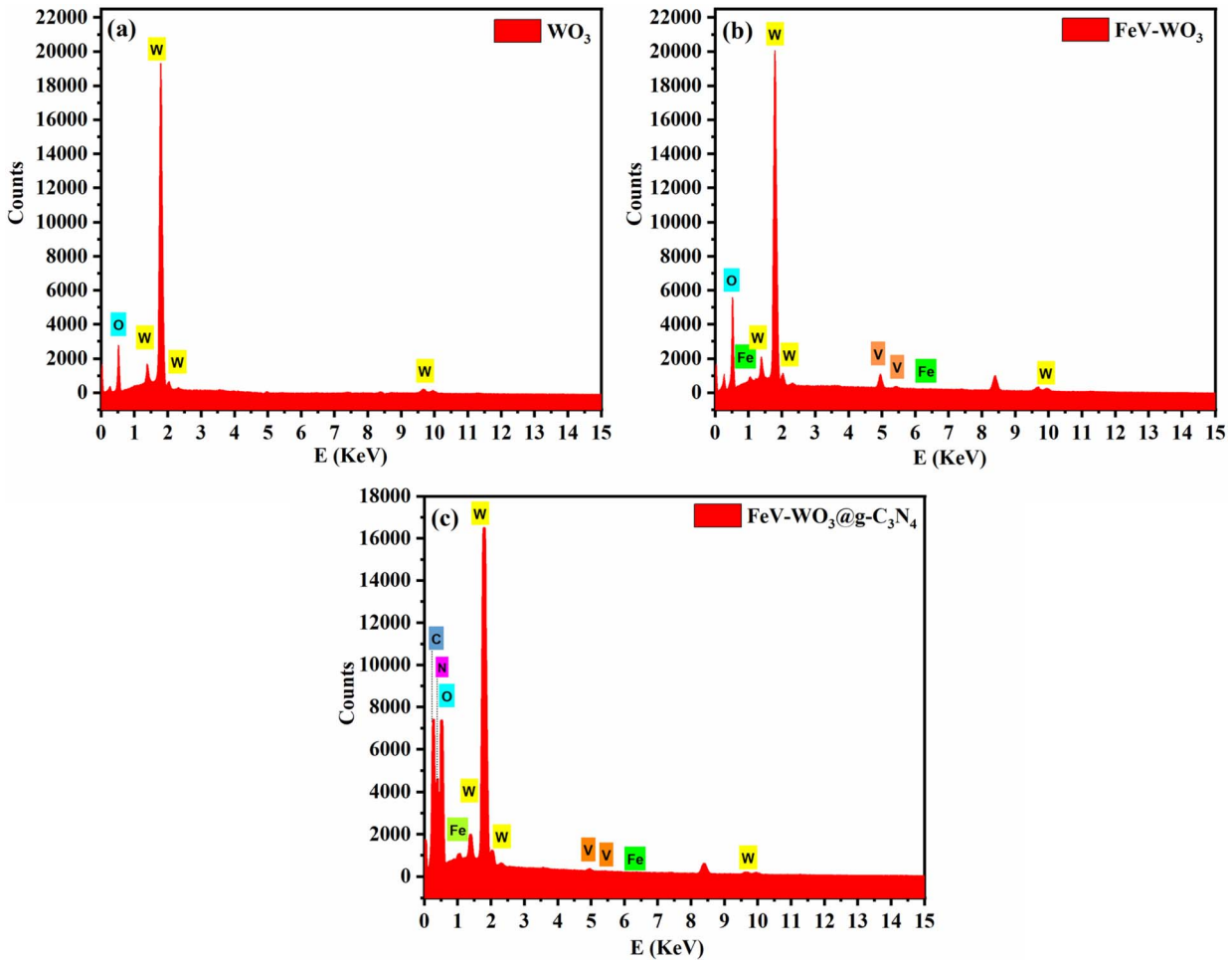

Fig. 5 EDS spectra of (a) WO_3, (b) FeV-WO_3, and (c) FeV-WO_3@g-C_3N_4 composite.

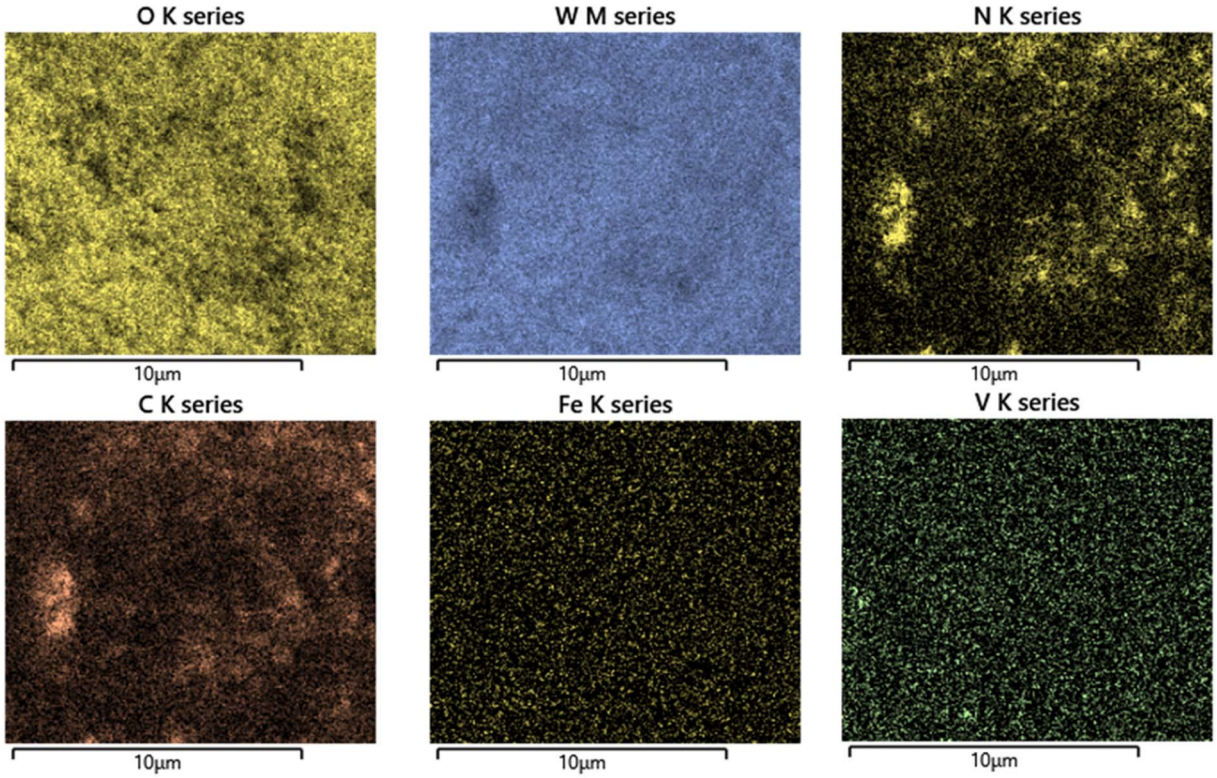

Fig. 6 EDS mapping of FeV-WO_3@g-C_3N_4 for O, W, N, C, Fe, and V.

3.3. Morphological analysis

The apparent shape, particle size distribution, texture, and dimensional nature of the produced nanostructures and composite were examined by FESEM analysis. FESEM images of the prepared samples are shown in Fig. 4(a)–(f). Fig. 4(a) and (b) exhibits the FESEM micrographs of WO_3 that shows asymmetrical 3D nanostructures with inhomogeneous particle sizes. The formation of asymmetric WO_3 nanostructures in the acidic medium can be explained with the help of the following eqn (1) and (2):[65]

$$Na_2WO_4 + 2HCl \rightarrow H_2WO_4 + 2NaCl \quad (1)$$

$$H_2WO_4 \rightarrow WO_3 + H_2O \quad (2)$$

In the acidic medium, H^+ and WO_4^{-2} combine to form H_2WO_4. Nucleation and crystal growth largely depends on the reaction conditions *i.e.*, pH, temperature, and reaction time.[66,67] At low pH (high concentration of H^+ ions) a large number of H_2WO_4 are formed. Supersaturation of H_2WO_4 is the driving force for nucleation.[68] At supersaturation, when the decomposition temperature is attained, H_2WO_4 degrades to several small 0D WO_3 nanoparticles. As the reaction time increases, these small nuclei in the absence of any surfactant aggregate together and grow into irregular shaped or asymmetric nanostructures.[69] FESEM image of FeV-WO_3 is represented in Fig. 4(c), which shows not much different morphology from WO_3. FESEM image of g-C_3N_4 depicted in Fig. 4(d) clearly shows that g-C_3N_4 is comprised of sheet like structure with irregular surface that increases the surface area of the material. Fig. 4(e) and (f) for FeV-WO_3@g-C_3N_4 shows that FeV-WO_3 nanostructures were dispersed on the surface of g-C_3N_4 sheets. The particles of FeV-WO_3 can easily attach to the surface of g-C_3N_4 due to the rough and uneven surface of g-C_3N_4. Such structures enhance the specific surface area that discloses more active sites and is more favorable for transfer of charges.[70] It is revealed that the overall shape of the composite shows an assemblage of FeV-WO_3 nanostructures with a loose stack of 2D sheets of g-C_3N_4.

3.4. Elemental analysis

In Fig. 5(a)–(c) EDS spectra of WO_3, FeV-WO_3, and FeV-WO_3@g-C_3N_4 are shown. EDS spectrum of WO_3 consists of W (at E = 1.38 keV, 1.81 keV, and 9.6 keV) and O (0.53 keV) elements. After the doping of Fe and V ions, new peaks appeared at 0.79 keV and 6.39 keV for Fe, and 4.9 keV and 5.4 keV for V. Finally, for FeV-WO_3@g-C_3N_4, C and N elements were observed at 0.23 keV and 0.38 keV. EDS mapping of FeV-WO_3@g-C_3N_4 is shown in Fig. 6 which clearly represents the presence of all required elements *i.e.*, O, W, N, C, Fe, and V.

3.5. XPS analysis

XPS measurements were performed to further analyze the elemental composition of the prepared samples. XPS spectra of WO_3, FeV-WO_3, and FeV-WO_3@g-C_3N_4 are depicted in Fig. 7(a)–(d). The overall survey spectrum of FeV-WO_3@g-C_3N_4 in Fig. 7(a) confirms the presence of all elements *i.e.*, W, O,

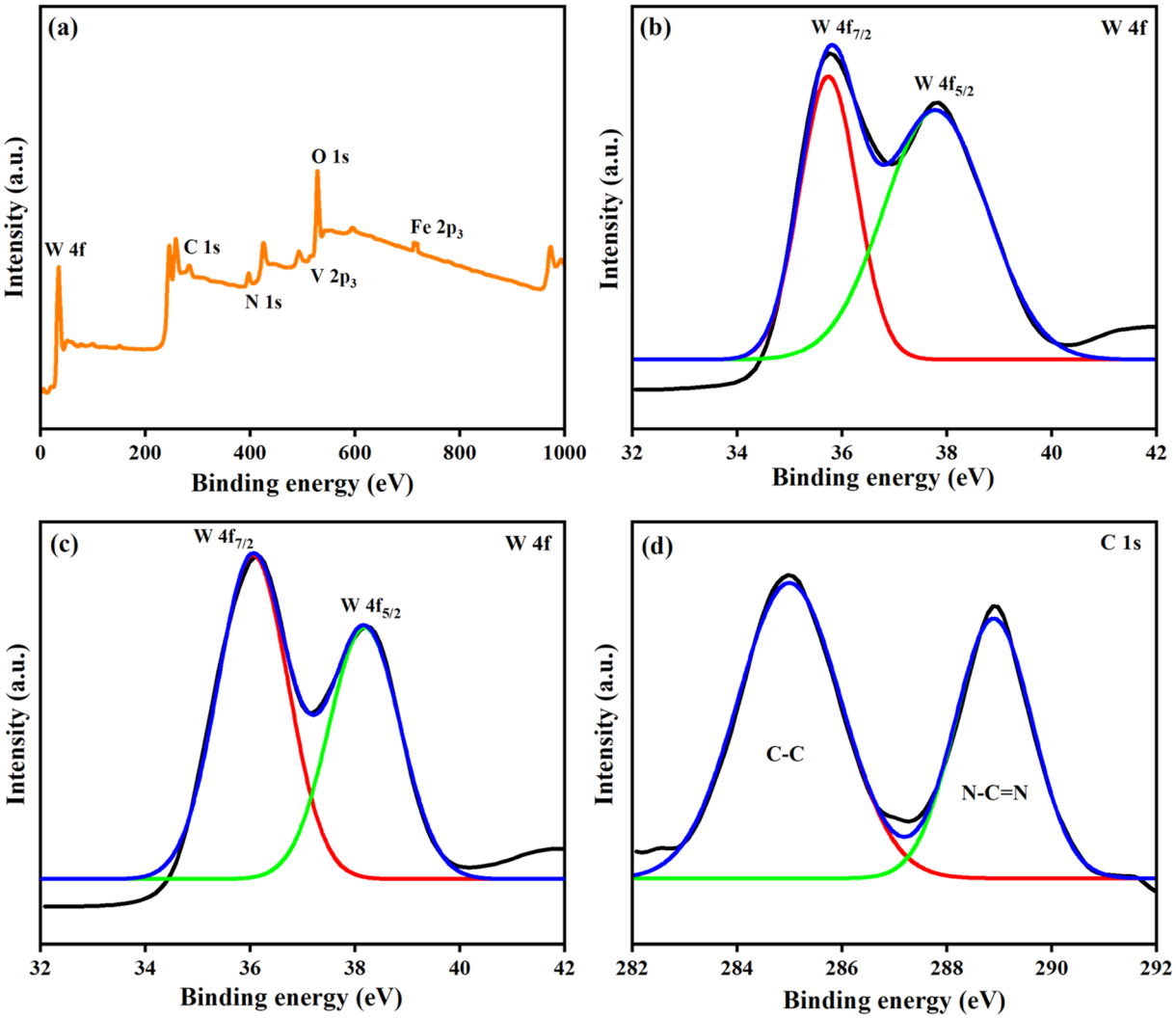

Fig. 7 (a) XPS survey spectrum of FeV-WO_3@g-C_3N_4. Deconvoluted high resolution XPS spectra of W 4f core levels of (b) WO_3, (c) FeV-WO_3, and C 1s core levels of (d) FeV-WO_3@g-C_3N_4.

Fe, V, C, and N. The primary doublet peaks of WO_3 at binding energies of 35.7 and 37.8 eV are possessed by W $4f_{7/2}$ and W $4f_{5/2}$ core levels, respectively (Fig. 7(b)).[71] These peaks represent that tungsten exhibits an oxidation state of W^{+6}. The difference in binding energy between the W $4f_{7/2}$ and W $4f_{5/2}$ levels is around 2.1 eV, which demonstrates excellent purity of WO_3. In XPS spectrum of FeV-WO_3 the binding energy of FeV-WO_3 nanoparticles was shifted slightly to lower energy side as compared to that of pure WO_3, which is attributed to the strong interaction of Fe and V with WO_3 (Fig. 7(c)). The XPS spectrum of FeV-WO_3@g-C_3N_4 confirms the presence of g-C_3N_4 (Fig. 7(d)). The peaks that emerged at 284.9 eV and 288.9 eV are attributed to the C–C and N–C=N bonds, respectively.[72]

3.6. Raman spectroscopy

Raman spectroscopy was used to investigate the local symmetry of the prepared materials. Raman spectra of WO_3, FeV-WO_3, and FeV-WO_3@g-C_3N_4 are exhibited in Fig. 8(a)–(c). In Fig. 8(a) peaks emerged at 127 cm^{-1}, 260 cm^{-1}, 324 cm^{-1}, 707 cm^{-1}, and 802 cm^{-1} in WO_3 spectra confirmed that the synthesized material exhibits monoclinic phase.[73] It is observed that peaks emerged in two pairs from 100–400 cm^{-1} and 600–900 cm^{-1} corresponding to O–W–O bending and stretching modes, respectively.[74] The monoclinic phase WO_3 exhibits a tilted and corner-shaped octahedral structure. The W atoms present on the off-center of the structure form 3 longer and 3 shorter bonds with the adjacent oxygen atom. This shows that the WO_3 tungsten ion has a coordination number '6' in the prepared sample.[75] Raman spectra of FeV-WO_3 showed similar pattern with almost same peak positions as exhibited by pure WO_3 (Fig. 8(b)). However, after the addition of g-C_3N_4, two new peaks appeared in Fig. 8(c) at 1358 cm^{-1} and 1570 cm^{-1} corresponding to D and G bands of g-C_3N_4.[76–78]

3.7. BET analysis

The N_2 adsorption/desorption isotherms with BJH pore size distribution plot are given in Fig. 9(a) and (b) for FeV-WO_3@g-C_3N_4. N_2 adsorption/desorption isotherms show typical type-IV

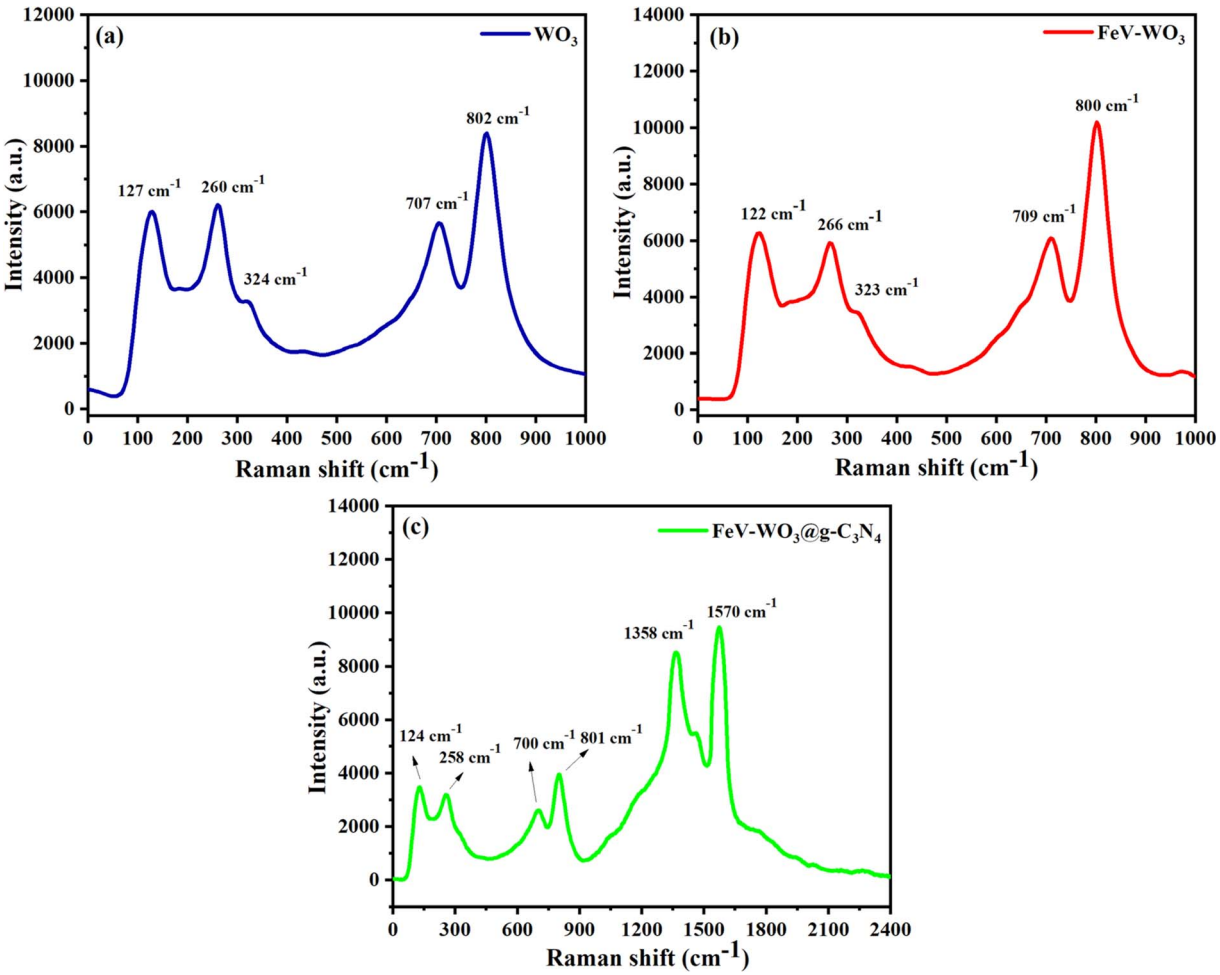

Fig. 8 Raman spectra of (a) WO_3, (b) FeV-WO_3, and (c) FeV-WO_3@g-C_3N_4 composite.

behavior with a small H_3 hysteresis loop in range of 0.8–1 (Fig. 9(a)).[79] Presence of H_3 hysteresis loop indicates the existence of mesopores in FeV-WO_3@g-C_3N_4 which can also be verified from pore size distribution plot. Based on adsorption/desorption isotherms, the BET surface area for FeV-WO_3@g-C_3N_4 was determined to be 40.2 $m^2\ g^{-1}$. This significant specific

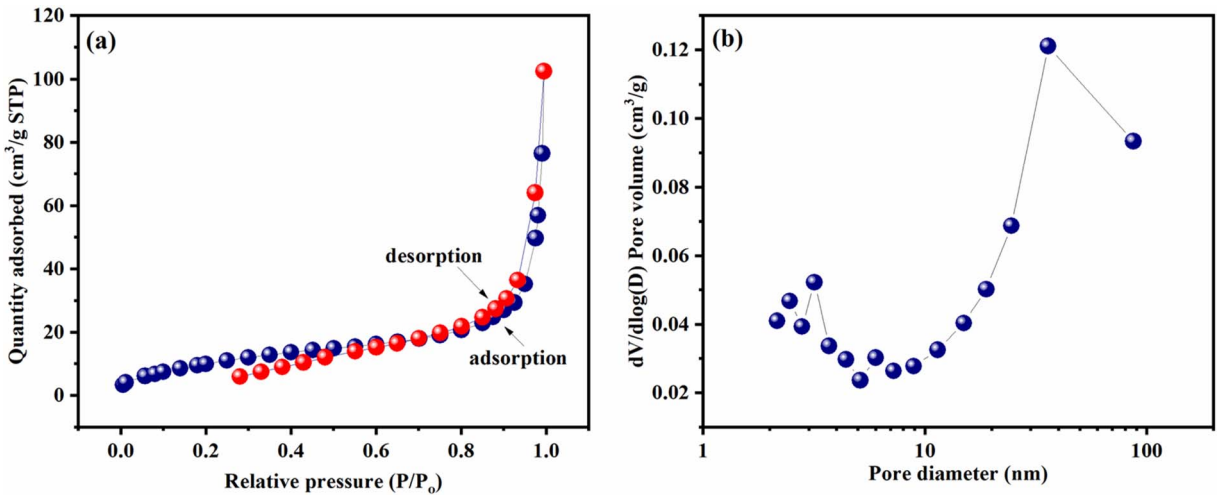

Fig. 9 (a) N_2 adsorption/desorption isotherms and (b) pore size distribution plot for FeV-WO_3@g-C_3N_4 composite.

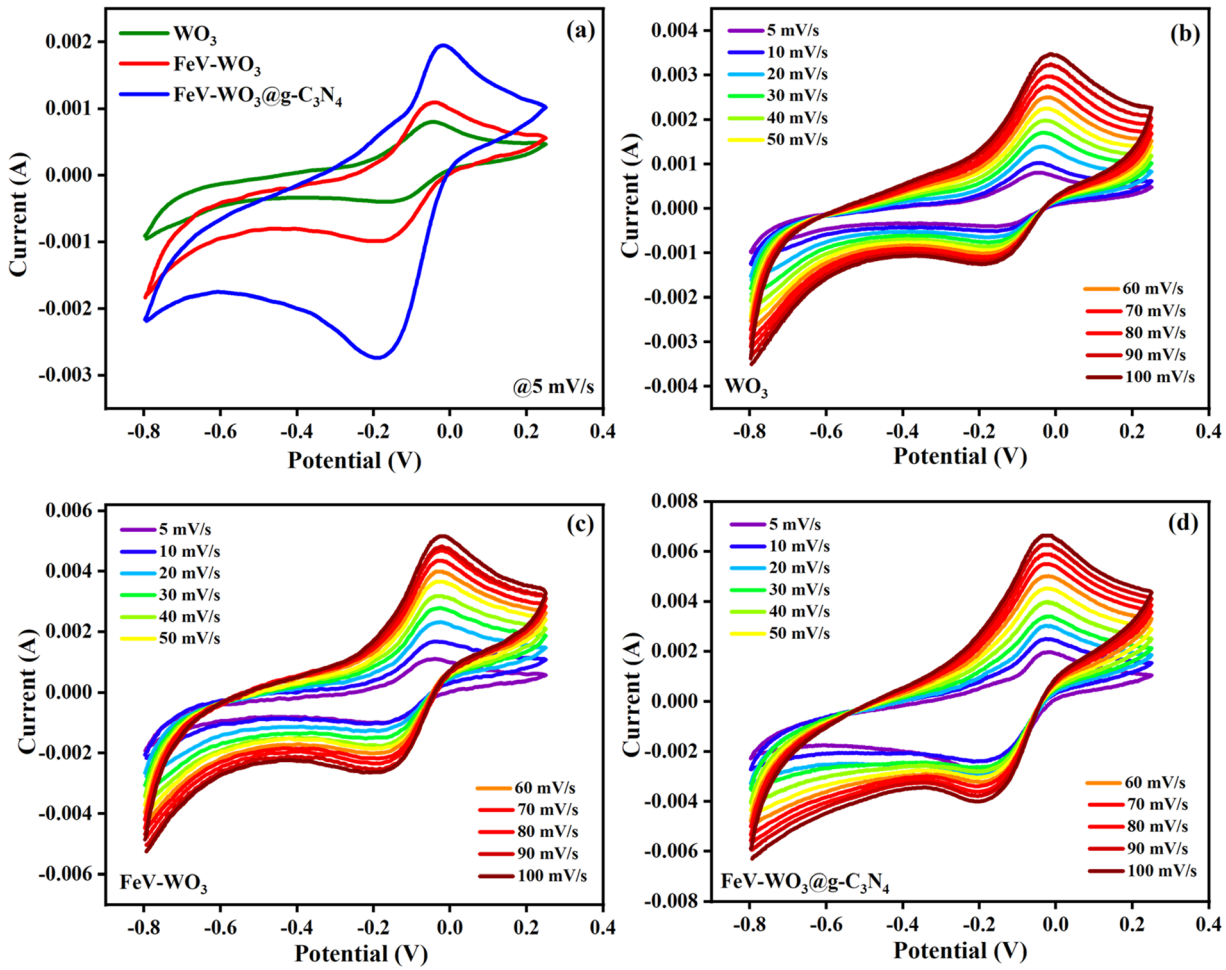

Fig. 10 CV profiles; (a) comparative CV curves of WO_3, FeV-WO_3, and FeV-WO_3@g-C_3N_4 taken at scan rate 5 mV s^{-1}, (b) CV curves of WO_3 at 5–100 mV s^{-1}, (c) CV curves of FeV-WO_3 at 5–100 mV s^{-1}, and (d) CV curves of FeV-WO_3@g-C_3N_4 at 5–100 mV s^{-1}.

surface area is certainly contributed by the g-C_3N_4 sheets.[80] Pore size distribution plot in Fig. 9(b) shows that the mesopores are centralized at ~3 nm and ~35 nm. These mesopores in FeV-WO_3@g-C_3N_4 develop ion diffusion channels and provide short ion diffusion paths with small resistance. The electrolyte ions can reach the interfacial sections of active electrode material through these mesopores which will lead to an enhancement of charge storage capacity of FeV-WO_3@g-C_3N_4.[81]

4. Electrochemical analysis

Electrochemical properties of all the prepared samples were tested by cyclic voltammetry (CV), galvanic charge–discharge (GCD), and electrochemical impedance spectroscopy (EIS) through a three electrode system in the electrolyte of 1 M Na_2SO_4. CV of WO_3, FeV-WO_3, and FeV-WO_3@g-C_3N_4 electrodes was performed at room temperature (26 °C) at different scan rates from 5 mV s^{-1} to 100 mV s^{-1} in Fig. 10(a)–(d). The potential window range of the CV profile was from −0.8 to 0.25 V (*vs.* Ag/AgCl). Fig. 10(a) shows comparative CV profiles of all samples at 5 mV s^{-1}. The CV curves exhibited duck shape with clear oxidation and reduction peaks which shows the pseudo-capacitive processes. During the charging process, Na^+ ions from the electrolyte were successfully incorporated onto the surface of electrodes and detached during the discharging process. The whole response mechanism can be illustrated by the following reaction in eqn (3):

$$WO_3 + xNa^+ \leftrightarrow xNa^+WO_3 \quad (3)$$

Further, it can be clearly observed that the composite FeV-WO_3@g-C_3N_4 exhibited higher current and CV area as compared to WO_3 and FeV-WO_3 which is related to higher electrodeposition and charge storage capacity, indicating the advantages of g-C_3N_4 for enhanced electrochemical performance. The current of the CV curves increased by increasing the scan rate in all cases (Fig. 10(b)–(d)) which shows direct relation between scan rate and current. CV curves remained uniform along *y*-axis with the increase in scan rate, and it also shows the good reversibility of redox processes.[82]

Specific capacitance of all the prepared electrodes at different scan rates *i.e.*, 5 mV s^{-1} to 100 mV s^{-1} was calculated by the following eqn (4):[83,84]

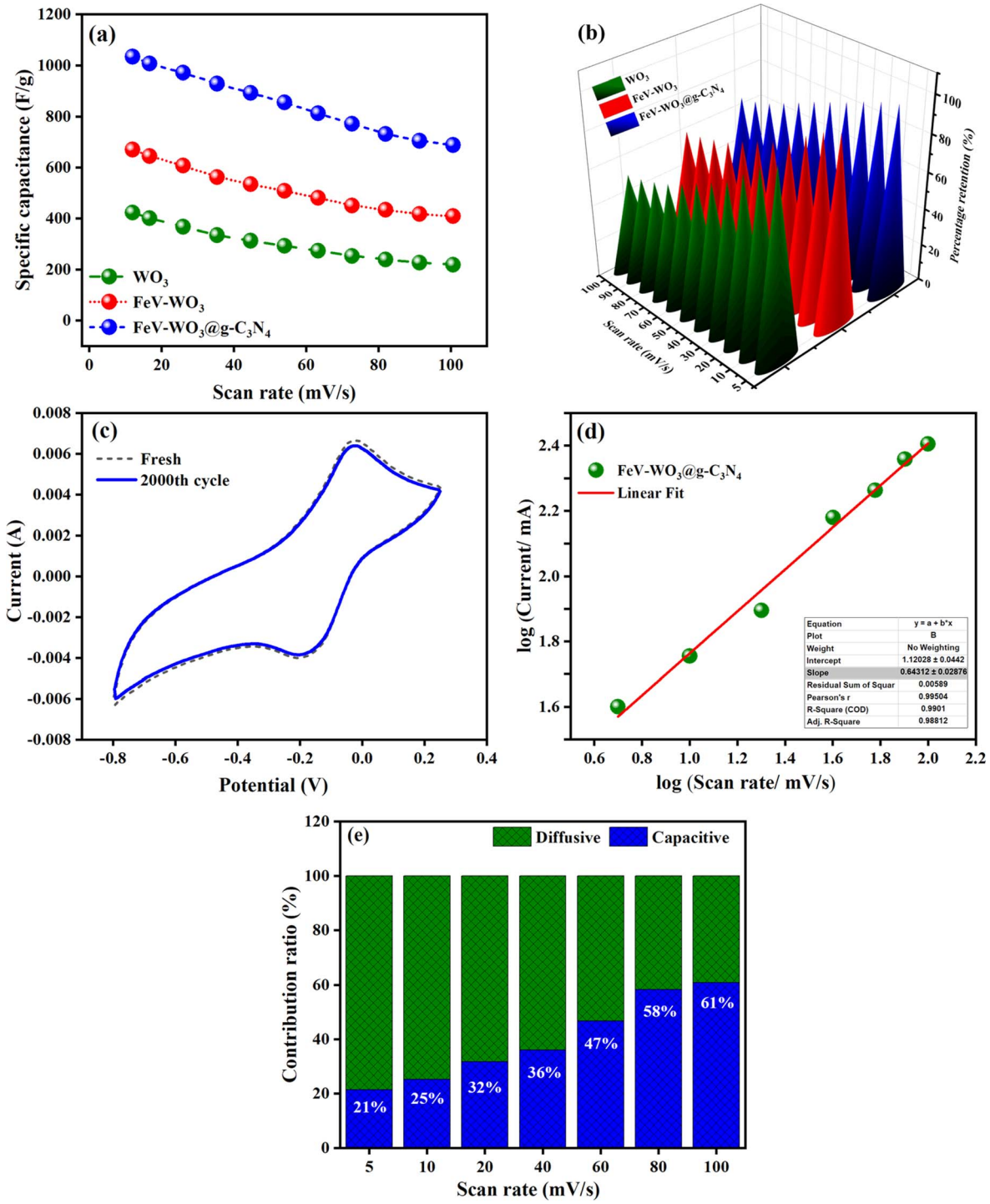

Fig. 11 (a) Specific capacitance of WO_3, FeV-WO_3, and FeV-WO_3@g-C_3N_4, (b) capacitance retention of WO_3, FeV-WO_3, and FeV-WO_3@g-C_3N_4 at scan rates (5–100 mV s^{-1}), (c) CV plot of FeV-WO_3@g-C_3N_4 for 2000 cycles to test stability at 100 mV s^{-1}, (d) log (scan rate) *vs.* log (current) for FeV-WO_3@g-C_3N_4, and (e) contribution ratio for FeV-WO_3@g-C_3N_4 at different scan rates.

$$C_{SP} = \int I\mathrm{d}V/(2 \times m \times \Delta V) \quad (4)$$

In the above formula, $I\mathrm{d}V$ is the area of CV loop, m is the mass of material deposited on electrode, and ΔV is applied potential limits.

The specific capacitance values calculated for WO_3, FeV-WO_3, and FeV-WO_3@g-C_3N_4 were found to be 422.76 F g^{-1}, 669.76 F g^{-1}, and 1033.68 F g^{-1}, respectively. As expected, FeV-WO_3@g-C_3N_4 has the highest specific capacitance value than WO_3 and FeV-WO_3 which is attributed to the increased

Table 1 Specific capacitance of all the prepared electrodes at different scan rates

Scan rate ($mV\ s^{-1}$)	Specific capacitance ($F\ g^{-1}$)		
	WO_3	FeV-WO_3	FeV-WO_3@g-C_3N_4
5	422.76	669.76	1033.68
10	400.38	645.06	1006.33
20	367.18	606.94	971.04
30	334.51	562.24	928.28
40	313.18	533.72	892.89
50	293.01	508.01	855.37
60	273.69	480.5	812.74
70	253.52	450.29	771.4
80	239.29	433.43	731.14
90	227.46	416.71	704.48
100	218.96	408.43	687.79

Table 2 Specific capacitance retention (%) for WO_3, FeV-WO_3, and FeV-WO_3@g-C_3N_4 at scan rate from 5–100 $mV\ s^{-1}$

Scan rate ($mV\ s^{-1}$)	Specific capacitance retention (%)		
	WO_3	FeV-WO_3	FeV-WO_3@g-C_3N_4
5	100	100	100
10	94.7	96.31	97.35
20	86.85	90.62	93.94
30	79.12	83.94	89.8
40	74.08	79.68	86.38
50	69.31	75.85	82.75
60	64.73	71.74	78.62
70	59.97	67.23	74.62
80	56.6	64.71	70.73
90	53.8	62.21	68.15
100	51.79	60.98	66.53

interactions between electrolyte solution and active sites due to the presence of g-C_3N_4. The electrons interact with g-C_3N_4, they quickly become entangled with WO_3 nanostructures, and the contact between the electrolyte and the working electrode is further strengthened by the structure of FeV-WO_3@g-C_3N_4 due to their synergistic effects. The morphology of the g-C_3N_4 speeds up the charge transfer between FeV-WO_3@g-C_3N_4 and current collector which reveals the efficient electrochemical performance of the FeV-WO_3@g-C_3N_4. Fig. 11(a) shows change in specific capacitance of electrode with scan rate. Specific capacitance values at different scan rates for all samples are presented in Table 1. The specific capacitance of electrodes degraded with the scan rate that is because at high scan rate the charge storage process is mostly limited to the surface of electrode due to the limited time. Capacitance retention values at different scan rates for all samples are presented in Table 2. As found, FeV-WO_3@g-C_3N_4 has highest capacitance retention value than WO_3 and FeV-WO_3 (Fig. 11(b)). The fundamental need of a supercapacitor for its real time implementation is the long-term cycle stability. In order to test the cyclic stability of the FeV-WO_3@g-C_3N_4, CV measurement was repeated at constant scan rate of 100 $mV\ s^{-1}$ in 1 M Na_2SO_4 electrolyte. The stability test of the electrode for 2000 cycles is shown in Fig. 11(c). It can be seen that our system can sustain approximately 2000 CV runs without any significant loss in the performance and distortion of CV shape. The percentage capacitance retention after 2000 cycles was determined to be 97.3%. A graph was plotted between log (scan rate) *vs.* log (current) for kinetic study of electrochemical measurements by Dunn's method (eqn (5) and (6)).[85]

$$i = av^b \tag{5}$$

Eqn (5) can be written as:

$$\log i = \log a + b \log v \tag{6}$$

By linear fitting, the slope value of anodic peak was found to be 0.643, represented in Fig. 11(d). This value of slope indicates that the dominant charge storage mechanism is diffusion controlled. Fig. 11(e) shows percentage contribution to charge storage at scan rates (5 to 100 $mV\ s^{-1}$). The bar graph clearly indicates that at high scan rates diffusion controlled processes become limited and mostly the surface of electrode takes part in charge storage process, as discussed beforehand.

The GCD plots of the prepared electrodes WO_3, FeV-WO_3, and FeV-WO_3@g-C_3N_4 at current density of 1 A g^{-1} and potential range of −0.8 to 0.25 V are represented in Fig. 12(a). GCD plots integrate to form quasi-triangular shape that represents electrochemical redox reactions at the electrode–electrolyte interface. Discharge time of the prepared electrodes WO_3, FeV-WO_3, and FeV-WO_3@g-C_3N_4 was 440 s, 649 s, and 867 s, respectively. FeV-WO_3@g-C_3N_4 exhibits a much longer discharge time than WO_3 and FeV-WO_3 indicating that it has greater charge storage capacity. The GCD plots of FeV-WO_3@g-C_3N_4 at different current densities *i.e.*, 1 A g^{-1}, 3 A g^{-1}, 5 A g^{-1}, 7 A g^{-1}, and 9 A g^{-1} are represented in Fig. 12(b). GCD plots demonstrate the good symmetry of the curves with no distortion in the shape of curves at high current densities. The coulombic efficiency for all electrodes was calculated by the following eqn (7):

$$\text{Coulombic efficiency}(\%) = \frac{T_d}{T_c} \times 100 \tag{7}$$

The calculated coulombic efficiency of WO_3, FeV-WO_3, and FeV-WO_3@g-C_3N_4 at 1 A g^{-1} was 80.1%, 92.1%, and 96.7%, respectively, as shown in Fig. 12(c). FeV-WO_3@g-C_3N_4 exhibits higher value of coulombic efficiency than WO_3 and FeV-WO_3 because of the presence of g-C_3N_4. Generally, higher value of internal resistance disturbs the coulombic efficiency value of energy storing material by consumption of a small amount of energy during the discharge time, that's why the energy released is always less than the amount of energy stored. The greater discharge current is related to the greater redox reactions that also tend to increase the internal resistance. The best coulombic efficiency value for composite illustrates uniformed charge and discharge current values and low internal

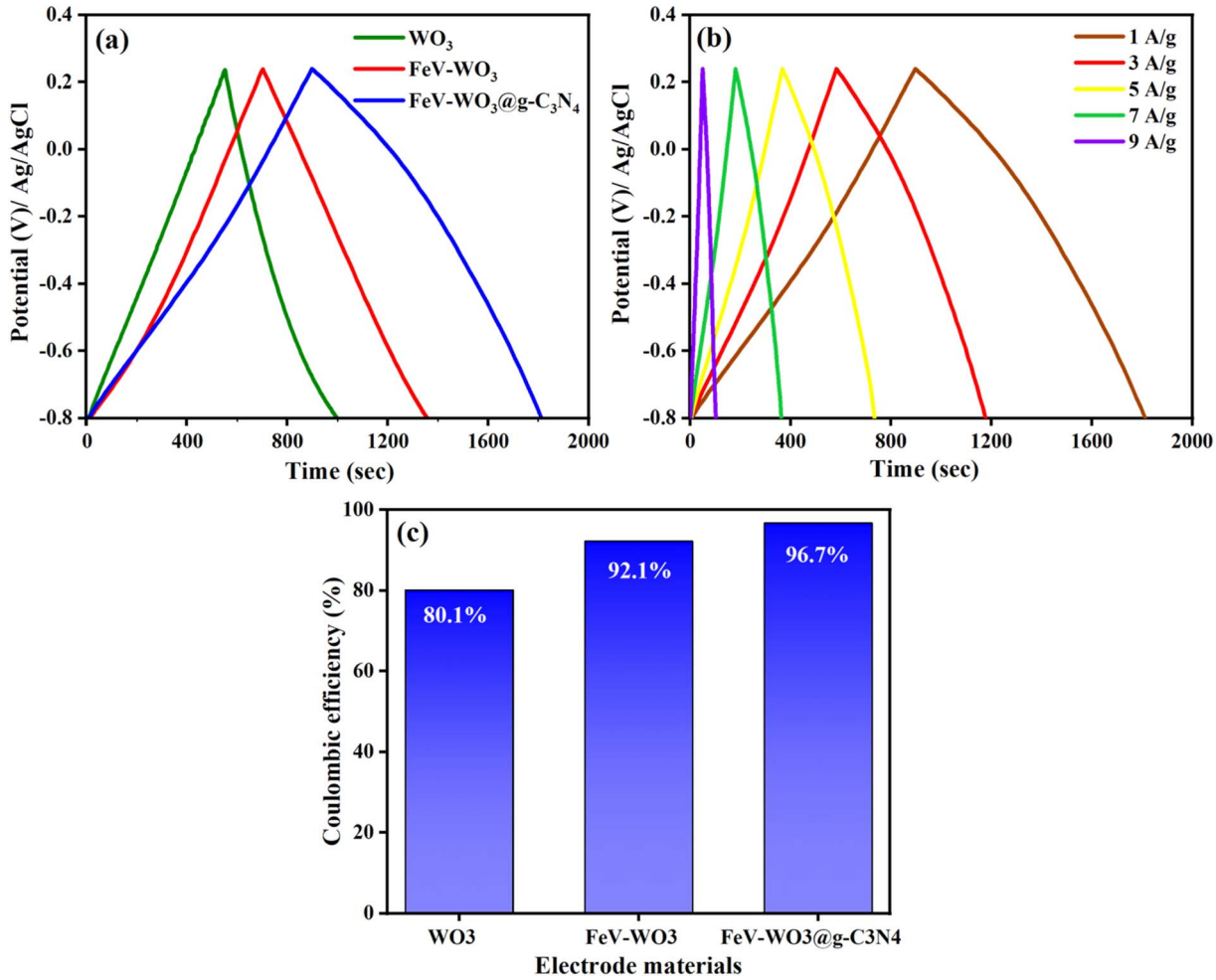

Fig. 12 (a) GCD curves of WO_3, FeV-WO_3, and FeV-WO_3@g-C_3N_4 at 1 A g^{-1}, (b) GCD plots of FeV-WO_3@g-C_3N_4 at different current densities, and (c) coulombic efficiency (%) of WO_3, FeV-WO_3, and FeV-WO_3@g-C_3N_4.

resistance.[3] Further, a comparison of different performance parameters (specific capacitance, cyclic stability, and coulombic efficiency) for FeV-WO_3@g-C_3N_4 with already reported similar electrode materials in Table 3 shows comparable or even greater electrochemical response of FeV-WO_3@g-C_3N_4.

EIS study is performed for the analysis of ion transfer and electrical conductivity of the prepared electrodes *i.e.*, WO_3, FeV-WO_3, and FeV-WO_3@g-C_3N_4. EIS measurements of the WO_3, FeV-WO_3, and FeV-WO_3@g-C_3N_4 in 1 M Na_2SO_4 were performed in the frequency range of 0.1 Hz–100 kHz, and corresponding Nyquist plots are presented in Fig. 13(a)–(c). Nyquist plot has two separate zones, the high frequency portion usually represented by an arc, and the low frequency zone by a sloped line.[92] The real impedance axis in Nyquist provides internal resistance of active material and the capacitance behavior of the electrode can be easily analyzed by the imaginary component of the Nyquist plot. The internal resistance or equivalent series resistance (E_{SR}) is represented by Nyquist's intersect with the real part of Nyquist plot. E_{SR} values of WO_3, FeV-WO_3, and FeV-WO_3@g-C_3N_4 were 2.22 Ω, 1.92 Ω, and 1.82 Ω, respectively. FeV-WO_3@g-C_3N_4 has low value of E_{SR} which

Table 3 Comparison of performance parameters of FeV-WO_3@g-C_3N_4 with already reported similar electrode materials

Electrode	Specific capacitance (F g^{-1})	Cyclic stability (%)	Coulombic efficiency (%)	Ref.
h-WO_3 nanoflakes	588	95.5%@5000 cycles	90.7%	86
WO_3 nanofibers	436	98%@5000 cycles	98%	87
Nb doped WO_3//MnO_2	126	90%@2000 cycles	96%	88
WO_3/graphene	761	99.2%@5000 cycles	98.2%	89
WO_3/carbon fiber	385	88%@1000 cycles	—	90
RGO–CNT-WO_3	691.38	89.09%@5000 cycles	98.4%	91
FeV-WO_3@g-C_3N_4	1033.68	97.3%@2000 cycles	96.7%	Current work

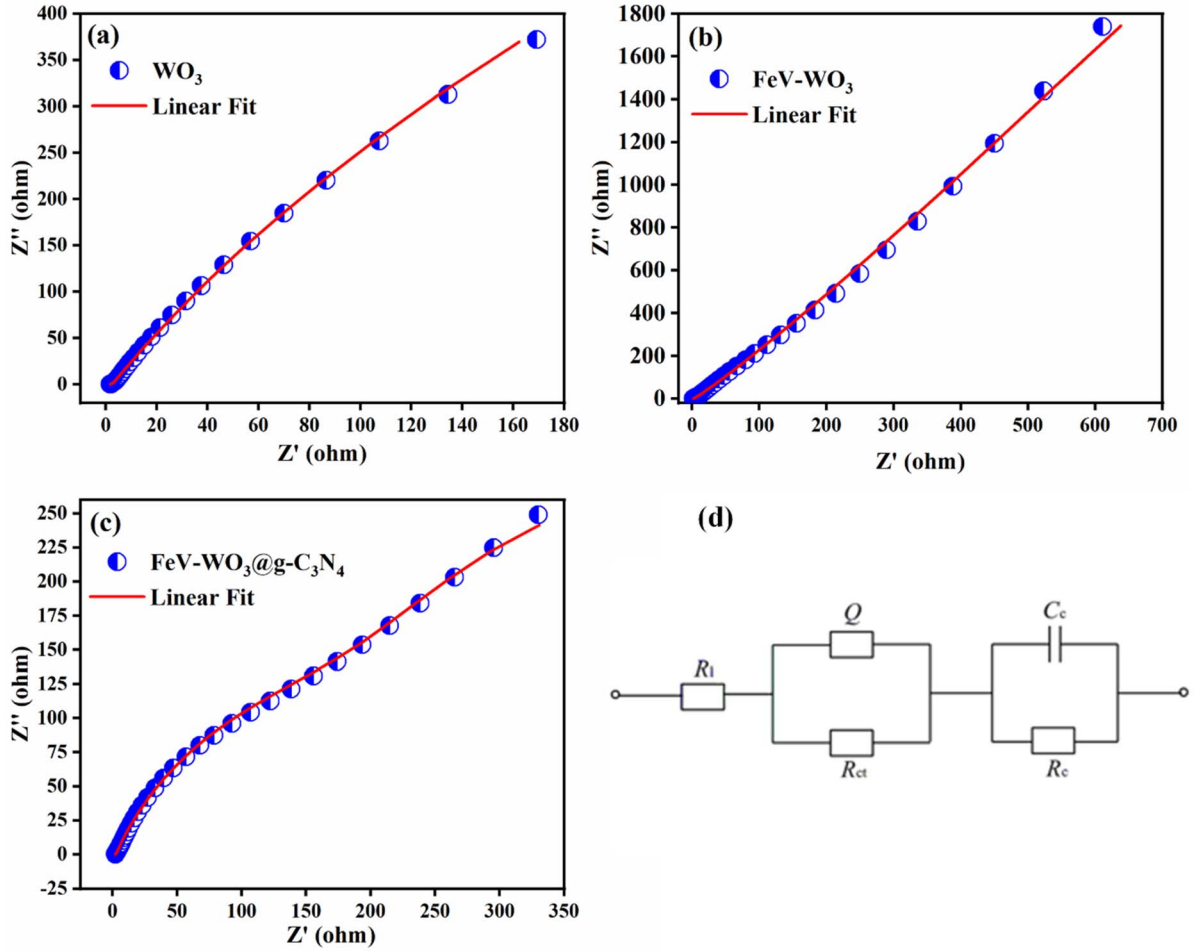

Fig. 13 Nyquist plot of (a) WO_3, (b) FeV-WO_3, (c) FeV-WO_3@g-C_3N_4, and (d) equivalent circuit diagram.

shows it contains low internal resistance and efficient electrical conductance. The charge-transfer resistance (R_{CT}) at electrode–electrolyte interface can be determined by the diameter of semicircle at high frequency region. In case of distorted semicircle, R_{CT} value can be determined by the extrapolation of arc on real axis. R_{CT} values for WO_3, FeV-WO_3, and FeV-WO_3@g-C_3N_4 were 1.53 Ω, 1.28 Ω, and 0.65 Ω, respectively. FeV-WO_3@g-C_3N_4 has a smaller value of charge transfer resistance than WO_3 and FeV-WO_3. The line at 45 °C parallel to the imaginary part at a higher frequency zone defines the diffusion or Warburg resistance (R_w) that is primarily related to the diffusive resistance of the electrolyte ions in electrode. Electrodes showing a vertical line towards the low frequency zone of the Nyquist plot illustrate the ideal behavior of the electrode for supercapacitors.[93] Equivalent circuit fitted to EIS data of prepared electrodes is shown in Fig. 13(d).

5. Conclusions

In short, the conductive material FeV-WO_3@g-C_3N_4 was prepared by wet chemical approach for supercapacitor study. When electrochemical studies were performed, prepared electrodes WO_3, FeV-WO_3, and FeV-WO_3@g-C_3N_4 revealed specific capacitance of 422.76 F g^{-1}, 669.76 F g^{-1}, and 1033.68 F g^{-1} at scan rate 5 mV s^{-1}, respectively in 1 M Na_2SO_4 electrolyte solution. FeV-WO_3@g-C_3N_4 exhibited a higher value of specific capacitance and also maintained its shape without any significant change in current even after 2000 cycles which confirms that it is the potential material for supercapacitor application. GCD study showed composite exhibited greater discharge time than other electrodes of about 867 s which reveals that it has greater charge storage ability. It is concluded from EIS measurements that FeV-WO_3@g-C_3N_4 has less electrochemical impedance than WO_3 and FeV-WO_3. The results demonstrated that FeV-WO_3@g-C_3N_4 has the best structural, morphological, and componential properties for optimal efficiency. Therefore, the remarkable electrochemical behavior of FeV-WO_3@g-C_3N_4 suggests that it can be employed as an effective supercapacitor electrode.

Conflicts of interest

There are no conflicts to declare.

Acknowledgements

The researchers would like to acknowledge Deanship of Scientific Research, Taif University for funding this work. Authors are

thankful to the Islamia University of Bahawalpur and HEC-Islamabad (Pakistan). Prof. Dr Sonia Zulfiqar is highly thankful for the support provided by the Statutory City of Ostrava, Czechia through Research Grant "Global Experts". Prof. Cochran and Zulfiqar are grateful for FESEM imaging, EDS mapping services, and XRD provided by Drs Warren Straszheim and Carolina Selvati of the Materials Analysis and Research Laboratory of the Iowa State University Office of Biotechnology.

References

1 N. Shaheen, M. Aadil, S. Zulfiqar, H. Sabeeh, P. O. Agboola, M. F. Warsi, M. F. Aly Aboud and I. Shakir, Fabrication of different conductive matrix supported binary metal oxides for supercapacitors applications, *Ceram. Int.*, 2021, **47**, 5273–5285.

2 S. Munir, A. Rasheed, S. Zulfiqar, M. Aadil, P. O. Agboola, I. Shakir and M. F. Warsi, Synthesis, characterization and photocatalytic parameters investigation of a new $CuFe_2O_4$/Bi_2O_3 nanocomposite, *Ceram. Int.*, 2020, **46**, 29182–29190.

3 K. Chaudhary, S. Zulfiqar, H. H. Somaily, M. Aadil, M. F. Warsi and M. Shahid, Rationally designed multifunctional Ti_3C_2 MXene@Graphene composite aerogel integrated with bimetallic selenides for enhanced supercapacitor performance and overall water splitting, *Electrochim. Acta*, 2022, **431**, 141103.

4 L. Dai, D. W. Chang, J. B. Baek and W. Lu, Carbon nanomaterials for advanced energy conversion and storage, *Small*, 2012, **8**, 1130–1166.

5 L. Qie, W. Chen, H. Xu, X. Xiong, Y. Jiang, F. Zou, X. Hu, Y. Xin, Z. Zhang and Y. Huang, Synthesis of functionalized 3D hierarchical porous carbon for high-performance supercapacitors, *Energy Environ. Sci.*, 2013, **6**, 2497–2504.

6 B. Ahmed, M. Shahid, D. H. Nagaraju, D. H. Anjum, M. N. Hedhili and H. N. Alshareef, Surface Passivation of MoO_3 Nanorods by Atomic Layer Deposition toward High Rate Durable Li Ion Battery Anodes, *ACS Appl. Mater. Interfaces*, 2015, **7**, 13154–13163.

7 T. Vignal, P. Banet, M. Pinault, R. Lafourcade, J. Descarpentries, L. Darchy, H. Hauf, C. Reynaud, M. Mayne-L'Hermite and P.-H. Aubert, Electropolymerized poly(3-methylthiophene) onto high density vertically aligned carbon nanotubes directly grown on aluminum substrate: application to electrochemical capacitors, *Electrochim. Acta*, 2020, **350**, 136377.

8 D.-W. Kim, K.-Y. Rhee and S.-J. Park, Synthesis of activated carbon nanotube/copper oxide composites and their electrochemical performance, *J. Alloys Compd.*, 2012, **530**, 6–10.

9 A. Rudge, I. Raistrick, S. Gottesfeld and J. P. Ferraris, A study of the electrochemical properties of conducting polymers for application in electrochemical capacitors, *Electrochim. Acta*, 1994, **39**, 273–287.

10 K. S. Ryu, K. M. Kim, N.-G. Park, Y. J. Park and S. H. Chang, Symmetric redox supercapacitor with conducting polyaniline electrodes, *J. Power Sources*, 2002, **103**, 305–309.

11 H. Wang, H. S. Casalongue, Y. Liang and H. Dai, $Ni(OH)_2$ Nanoplates Grown on Graphene as Advanced Electrochemical Pseudocapacitor Materials, *J. Am. Chem. Soc.*, 2010, **132**, 7472–7477.

12 J. Noh, C.-M. Yoon, Y. K. Kim and J. Jang, High performance asymmetric supercapacitor twisted from carbon fiber/MnO_2 and carbon fiber/MoO_3, *Carbon*, 2017, **116**, 470–478.

13 Y. Zhang, H. Li, L. Pan, T. Lu and Z. Sun, Capacitive behavior of graphene–ZnO composite film for supercapacitors, *J. Electroanal. Chem.*, 2009, **634**, 68–71.

14 S.-I. Kim, J.-S. Lee, H.-J. Ahn, H.-K. Song and J.-H. Jang, Facile route to an efficient NiO supercapacitor with a three-dimensional nanonetwork morphology, *ACS Appl. Mater. Interfaces*, 2013, **5**, 1596–1603.

15 S. I. Kim, J. S. Lee, H. J. Ahn, H. K. Song and J. H. Jang, Facile route to an efficient NiO supercapacitor with a three-dimensional nanonetwork morphology, *ACS Appl. Mater. Interfaces*, 2013, **5**, 1596–1603.

16 S. K. Meher and G. R. Rao, Ultralayered Co_3O_4 for high-performance supercapacitor applications, *J. Phys. Chem. C*, 2011, **115**, 15646–15654.

17 M. You, W. Zhang, X. Yan, H. Jiang, J. Miao, Y. Li, W. Zhou, Y. Zhu and X. Cheng, V_2O_5 nanosheets assembled on 3D carbon fiber felt as a free-standing electrode for flexible asymmetric supercapacitor with remarkable energy density, *Ceram. Int.*, 2021, **47**, 3337–3345.

18 S. K. Shinde, S. M. Mohite, A. A. Kadam, H. M. Yadav, G. S. Ghodake, K. Y. Rajpure, D. S. Lee and D. Y. Kim, Effect of deposition parameters on spray pyrolysis synthesized CuO nanoparticle thin films for higher supercapacitor performance, *J. Electroanal. Chem.*, 2019, **850**, 113433.

19 D. Wu, X. Xie, Y. Ma, J. Zhang, C. Hou, X. Sun, X. Yang, Y. Zhang, H. Kimura and W. Du, Morphology controlled hierarchical NiS/carbon hexahedrons derived from nitrilotriacetic acid-assembly strategy for high-performance hybrid supercapacitors, *Chem. Eng. J.*, 2022, **433**, 133673.

20 J. Li, D. Chen and Q. Wu, Facile synthesis of CoS porous nanoflake for high performance supercapacitor electrode materials, *J. Energy Storage*, 2019, **23**, 511–514.

21 X. Lu, D. Zheng, T. Zhai, Z. Liu, Y. Huang, S. Xie and Y. Tong, Facile synthesis of large-area manganese oxide nanorod arrays as a high-performance electrochemical supercapacitor, *Energy Environ. Sci.*, 2011, **4**, 2915–2921.

22 X.-H. Xia, J.-P. Tu, Y.-J. Mai, X.-L. Wang, C.-D. Gu and X.-B. Zhao, Self-supported hydrothermal synthesized hollow Co_3O_4 nanowire arrays with high supercapacitor capacitance, *J. Mater. Chem.*, 2011, **21**, 9319–9325.

23 D. Feng, Y. Lv, Z. Wu, Y. Dou, L. Han, Z. Sun, Y. Xia, G. Zheng and D. Zhao, Free-Standing Mesoporous Carbon Thin Films with Highly Ordered Pore Architectures for Nanodevices, *J. Am. Chem. Soc.*, 2011, **133**, 15148–15156.

24 H. Jiang, L. Yang, C. Li, C. Yan, P. S. Lee and J. Ma, High–rate electrochemical capacitors from highly graphitic carbon–tipped manganese oxide/mesoporous carbon/manganese oxide hybrid nanowires, *Energy Environ. Sci.*, 2011, **4**, 1813–1819.

25 S. Guo, S. Dong and E. Wang, Constructing carbon-nanotube/metal hybrid nanostructures using homogeneous TiO_2 as a spacer, *Small*, 2008, **4**, 1133–1138.
26 H. Jiang, T. Zhao, J. Ma, C. Yan and C. Li, Ultrafine manganese dioxide nanowire network for high-performance supercapacitors, *Chem. Commun.*, 2011, **47**, 1264–1266.
27 X. Lu, T. Zhai, X. Zhang, Y. Shen, L. Yuan, B. Hu, L. Gong, J. Chen, Y. Gao and J. Zhou, WO_{3-x}@ Au@ MnO_2 core–shell nanowires on carbon fabric for high-performance flexible supercapacitors, *Adv. Mater.*, 2012, **24**, 938–944.
28 J. H. Lee, K.-W. Kim, J. K. Kim and U. Jeong, DC Voltage Modulation for Integrated Self-Charging Power Systems of Triboelectric Nanogenerators and Ion Gel/WO_3 Supercapacitors, *ACS Appl. Electron. Mater.*, 2020, **2**, 2550–2557.
29 S. Wang, H. Xu, T. Hao, P. Wang, X. Zhang, H. Zhang, J. Xue, J. Zhao and Y. Li, In situ XRD and operando spectra-electrochemical investigation of tetragonal WO_{3-x} nanowire networks for electrochromic supercapacitors, *NPG Asia Mater.*, 2021, **13**, 51.
30 J. Xu, T. Ding, J. Wang, J. Zhang, S. Wang, C. Chen, Y. Fang, Z. Wu, K. Huo and J. Dai, Tungsten oxide nanofibers self-assembled mesoscopic microspheres as high-performance electrodes for supercapacitor, *Electrochim. Acta*, 2015, **174**, 728–734.
31 P. Yang, P. Sun, L. Du, Z. Liang, W. Xie, X. Cai, L. Huang, S. Tan and W. Mai, Quantitative Analysis of Charge Storage Process of Tungsten Oxide that Combines Pseudocapacitive and Electrochromic Properties, *J. Phys. Chem. C*, 2015, **119**, 16483–16489.
32 M. Qiu, P. Sun, L. Shen, K. Wang, S. Song, X. Yu, S. Tan, C. Zhao and W. Mai, WO_3 nanoflowers with excellent pseudo-capacitive performance and the capacitance contribution analysis, *J. Mater. Chem. A*, 2016, **4**, 7266–7273.
33 J. Chu, D. Lu, X. Wang, X. Wang and S. Xiong, WO_3 nanoflower coated with graphene nanosheet: synergetic energy storage composite electrode for supercapacitor application, *J. Alloys Compd.*, 2017, **702**, 568–572.
34 D. J. Ham, A. Phuruangrat, S. Thongtem and J. S. Lee, Hydrothermal synthesis of monoclinic WO_3 nanoplates and nanorods used as an electrocatalyst for hydrogen evolution reactions from water, *Chem. Eng. J.*, 2010, **165**, 365–369.
35 J. Li, X. Liu, J. Cui and J. Sun, Hydrothermal synthesis of self-assembled hierarchical tungsten oxides hollow spheres and their gas sensing properties, *ACS Appl. Mater. Interfaces*, 2015, **7**, 10108–10114.
36 H. Zhang, J. Yang, D. Li, W. Guo, Q. Qin, L. Zhu and W. Zheng, Template-free facile preparation of monoclinic WO_3 nanoplates and their high photocatalytic activities, *Appl. Surf. Sci.*, 2014, **305**, 274–280.
37 W.-J. Li and Z.-W. Fu, Nanostructured WO_3 thin film as a new anode material for lithium-ion batteries, *Appl. Surf. Sci.*, 2010, **256**, 2447–2452.
38 N. Prabhu, S. Agilan, N. Muthukumarasamy and T. S. Senthil, Enhanced photovoltaic performance of WO_3 nanoparticles added dye sensitized solar cells, *J. Mater. Sci.: Mater. Electron.*, 2014, **25**, 5288–5295.
39 P. M. Rao, I. S. Cho and X. Zheng, Flame synthesis of WO_3 nanotubes and nanowires for efficient photoelectrochemical water-splitting, *Proc. Combust. Inst.*, 2013, **34**, 2187–2195.
40 Y. Li, X. Zhai, Y. Liu, H. Wei, J. Ma, M. Chen, X. Liu, W. Zhang, G. Wang and F. Ren, WO_3-based materials as electrocatalysts for hydrogen evolution reaction, *Front. Mater.*, 2020, **7**, 105.
41 A. K. Nayak, E. Enhtuwshin, S. J. Kim and H. Han, Facile Synthesis of N-Doped WS_2 Nanosheets as an Efficient and Stable Electrocatalyst for Hydrogen Evolution Reaction in Acidic Media, *Catalysts*, 2020, **10**, 12–38.
42 W. Liu, P. Geng, S. Li, W. Liu, D. Fan, H. Lu, Z. Lu and Y. Liu, Tuning electronic configuration of WP_2 nanosheet arrays via nickel doping for high-efficiency hydrogen evolution reaction, *J. Energy Chem.*, 2021, **55**, 17–24.
43 J. Zhang, H. Ma and L. Zhifeng, Highly efficient photocatalyst based on all oxides WO_3/Cu_2O heterojunction for photoelectrochemical water splitting, *Appl. Catal., B*, 2017, **201**, 84–91.
44 S. P. Gupta, V. B. Patil, N. L. Tarwal, S. D. Bhame, S. W. Gosavi, I. S. Mulla, D. J. Late, S. S. Suryavanshi and P. S. Walke, Enhanced energy density and stability of self-assembled cauliflower of Pd doped monoclinic WO_3 nanostructure supercapacitor, *Mater. Chem. Phys.*, 2019, **225**, 192–199.
45 R. D. Kumar, Y. Andou and S. Karuppuchamy, Synthesis and characterization of nanostructured Ni-WO_3 and $NiWO_4$ for supercapacitor applications, *J. Alloys Compd.*, 2016, **654**, 349–356.
46 A. Martin and V. N. Kalevaru, Heterogeneously catalyzed ammoxidation: a valuable tool for one-step synthesis of nitriles, *ChemCatChem*, 2010, **2**, 1504–1522.
47 Y.-Y. Yeh, W.-H. Chiang and W.-R. Liu, Synthesis of few-layer WS_2 by jet cavitation as anode material for lithium ion batteries, *J. Alloys Compd.*, 2019, **775**, 1251–1258.
48 K. Peng, H. Wang, X. Li, J. Wang, Z. Cai, L. Su and X. Fan, Emerging WS(2)/montmorillonite composite nanosheets as an efficient hydrophilic photocatalyst for aqueous phase reactions, *Sci. Rep.*, 2019, **9**, 16325.
49 S. Karthikeyan, M. Selvapandiyan, P. Sasikumar, M. Parthibavaraman, S. Nithiyanantham and V. T. Srisuvetha, Investigation on the properties of vanadium doping WO_3 nanostructures by hydrothermal method, *Mater. Sci. Energy Technol.*, 2022, **5**, 411–415.
50 M. Devi, S. Yesmin, B. Das, S. S. Dhar and R. Dasgupta, Efficient Oxygen Doping of Graphitic Carbon Nitride by Green Microwave Irradiation for High-Performance Supercapacitor Electrode Material, *Energy Fuels*, 2023, **37**, 3247–3259.
51 B. S. Reghunath, S. Rajasekaran, S. D. KR, B. Saravanakumar, J. J. William, D. Pinheiro, D. Govindarajan and S. Kheawhom, Fabrication of bismuth ferrite/graphitic carbon nitride/N-doped graphene quantum dots composite

for high performance supercapacitors, *J. Phys. Chem. Solids*, 2022, **171**, 110985.

52 B. Rani, A. K. Nayak and N. K. Sahu, Electrochemical supercapacitor application of $CoFe_2O_4$ nanoparticles decorated over graphitic carbon nitride, *Diamond Relat. Mater.*, 2021, **120**, 108671.

53 C. T. Altaf, T. O. Colak, F. Lufrano, G. S. Unal, N. D. Sankir and M. Sankir, Graphitic carbon nitride/zinc oxide composite electrodes for all-solid-state photo-supercapacitor with ion exchange membrane separator, *J. Energy Storage*, 2022, **55**, 105784.

54 R. Santos, R. S. Babu, M. Devendiran, D. Haddad and A. De Barros, Facile synthesis of transition metal (M = Cu, Co) oxide grafted graphitic carbon nitride nanosheets for high performance asymmetric supercapacitors, *Mater. Lett.*, 2022, **308**, 131156.

55 S. M. El-Bahy, J. Arshad, S. Munir, K. Chaudhary, D. Alhashmialameer, D. R. Eddy, M. F. Warsi and M. Shahid, Improved photocatalytic performance of a new silver doped $BiSbO_4$ photocatalyst, *Ceram. Int.*, 2022, **48**, 23914–23920.

56 A. Irshad, H. H. Somaily, S. Zulfiqar, M. F. Warsi, M. I. Din, K. Chaudhary and M. Shahid, Silver doped $NiAl_2O_4$ nanoplates anchored onto the 2D graphitic carbon nitride sheets for high-performance supercapacitor applications, *J. Alloys Compd.*, 2023, **934**, 167705.

57 I. Mustafa, B. Basha, S. Zulfiqar, A. Tahir, F. Hanif, M. Al-Buriahi, M. Akhtar and K. Chaudhary, L-Cysteine functionalized coral-like Ag doped MnO_2 nanostructures for the real-time electrochemical detection of lead and cadmium ions, *Mater. Chem. Phys.*, 2023, **305**, 127991.

58 K. Chaudhary, M. Aadil, S. Zulfiqar, S. Ullah, S. Haider, P. O. Agboola, M. F. Warsi and I. Shakir, Graphene oxide and reduced graphene oxide supported ZnO nanochips for removal of basic dyes from the industrial effluents, *Fullerenes, Nanotubes Carbon Nanostruct.*, 2021, **29**, 915–928.

59 T. Tahir, K. Chaudhary, M. F. Warsi, M. S. Saif, I. A. Alsafari, I. Shakir, P. O. Agboola, S. Haider and S. Zulfiqar, Synthesis of sponge like Gd^{3+} doped vanadium oxide/2D MXene composites for improved degradation of industrial effluents and pathogens, *Ceram. Int.*, 2022, **48**, 1969–1980.

60 H. Chaudhary, K. Chaudhary, S. Zulfiqar, M. S. Saif, I. A. Alsafari, I. Shakir, P. O. Agboola, M. Safdar and M. F. Warsi, Fabrication of reduced Graphene Oxide supported Gd^{3+} doped V_2O_5 nanorod arrays for superior photocatalytic and antibacterial activities, *Ceram. Int.*, 2021, **47**, 32521–32533.

61 K. Chaudhary, N. Shaheen, S. Zulfiqar, M. I. Sarwar, M. Suleman, P. O. Agboola, I. Shakir and M. F. Warsi, Binary WO_3–ZnO nanostructures supported rGO ternary nanocomposite for visible light driven photocatalytic degradation of methylene blue, *Synth. Met.*, 2020, **269**, 116526.

62 M. F. Warsi, K. Chaudhary, S. Zulfiqar, A. Rahman, I. A. Al Safari, H. M. Zeeshan, P. O. Agboola, M. Shahid and M. Suleman, Copper and silver substituted MnO_2 nanostructures with superior photocatalytic and antimicrobial activity, *Ceram. Int.*, 2022, **48**, 4930–4939.

63 S. Sunasee, K. H. Leong, K. T. Wong, G. Lee, S. Pichiah, I. Nah, B.-H. Jeon, Y. Yoon and M. Jang, Sonophotocatalytic degradation of bisphenol A and its intermediates with graphitic carbon nitride, *Environ. Sci. Pollut. Res.*, 2019, **26**, 1082–1093.

64 I. A. Alsafari, K. Chaudhary, M. F. Warsi, A.-Z. Warsi, M. Waqas, M. Hasan, A. Jamil and M. Shahid, A facile strategy to fabricate ternary WO_3/CuO/rGO nano-composite for the enhanced photocatalytic degradation of multiple organic pollutants and antimicrobial activity, *J. Alloys Compd.*, 2023, **938**, 168537.

65 F. Mehmood, J. Iqbal, T. Jan, W. Ahmed, W. Ahmed, A. Arshad, Q. Mansoor, S. Z. Ilyas, M. Ismail and I. Ahmad, Effect of Sn doping on the structural, optical, electrical and anticancer properties of WO_3 nanoplates, *Ceram. Int.*, 2016, **42**, 14334–14341.

66 C. Pang, J. Luo, Z. Guo, M. Guo and T. Hou, Inhibition of tungsten particle growth during reduction of V-doped WO_3 nanoparticles prepared by co-precipitation method, *Int. J. Refract. Met. Hard Mater.*, 2010, **28**, 343–348.

67 C.-S. Wu, Hydrothermal fabrication of WO_3 hierarchical architectures: structure, growth and response, *Nanomaterials*, 2015, **5**, 1250–1255.

68 G. Cao, *Nanostructures & Nanomaterials: Synthesis, Properties & Applications*, Imperial College Press, 2004.

69 Y. Yu, W. Zeng, M. Xu and X. Peng, Hydrothermal synthesis of $WO_3 \cdot H_2O$ with different nanostructures from 0D to 3D and their gas sensing properties, *Phys. E*, 2016, **79**, 127–132.

70 J. Yu, S. Xiong, B. Wang, R. Wang, B. He, J. Jin, H. Wang and Y. Gong, Constructing boron-doped graphitic carbon nitride with 2D/1D porous hierarchical architecture and efficient N_2 photofixation, *Colloids Surf., A*, 2023, **656**, 130481.

71 Y. Huang, Y. Li, G. Zhang, W. Liu, D. Li, R. Chen, F. Zheng and H. Ni, Simple synthesis of 1D, 2D and 3D WO_3 nanostructures on stainless steel substrate for high-performance supercapacitors, *J. Alloys Compd.*, 2019, **778**, 603611.

72 S. Gong, Z. Jiang, S. Zhu, J. Fan, Q. Xu and Q. Min, The synthesis of graphene-TiO_2/g-C_3N_4 super-thin heterojunctions with enhanced visible-light photocatalytic activities, *J. Nanopart. Res.*, 2018, **20**, 1–13.

73 S. V. Mohite, V. V. Ganbavle and K. Y. Rajpure, Solar photoelectrocatalytic activities of rhodamine-B using sprayed WO_3 photoelectrode, *J. Alloys Compd.*, 2016, **655**, 106–113.

74 L. Mohan, A. V. Avani, P. Kathirvel, R. Marnadu, R. Packiaraj, J. R. Joshua, N. Nallamuthu, M. Shkir and S. Saravanakumar, Investigation on structural, morphological and electrochemical properties of Mn doped WO_3 nanoparticles synthesized by co-precipitation method for supercapacitor applications, *J. Alloys Compd.*, 2021, **882**, 160670.

75 H. Habazaki, Y. Hayashi and H. Konno, Characterization of electrodeposited WO_3 films and its application to

electrochemical wastewater treatment, *Electrochim. Acta*, 2002, **47**, 4181–4188.

76 M. Sumathi, A. Prakasam and P. Anbarasan, Fabrication of hexagonal disc shaped nanoparticles g-C_3N_4/NiO heterostructured nanocomposites for efficient visible light photocatalytic performance, *J. Cluster Sci.*, 2019, **30**, 757–766.

77 G. Wu, Q. Liu, J. Wang, Z. Cai, H. Li, T. Zhang, R. Lu, P. Li, J. Han and W. Xing, Synthesis of silver-based composite photocatalysis material and its visible-light-driven photocatalytic degradation of dye pollutants, *Fresenius Environ. Bull.*, 2021, **30**, 9696–9706.

78 M. Sumathi, A. Prakasam and P. Anbarasan, High capable visible light driven photocatalytic activity of WO_3/g-C_3N_4 hetrostructure catalysts synthesized by a novel one step microwave irradiation route, *J. Mater. Sci.: Mater. Electron.*, 2019, **30**, 3294–3304.

79 K. Chaudhary, B. Basha, S. Zulfiqar, S. Yousaf, E. W. Cochran, M. Al-Buriahi, M. F. Warsi and M. Shahid, 3D cellular lattice like-Ti_3C_2 MXene based aerogels embedded with metal selenides particles for energy storage and water splitting applications, *Fuel*, 2023, **351**, 128856.

80 Z. Zhao, H. Ma, M. Feng, Z. Li, D. Cao and Z. Guo, In situ preparation of WO_3/g-C_3N_4 composite and its enhanced photocatalytic ability, a comparative study on the preparation methods, *Eng. Sci.*, 2019, **7**, 52–58.

81 A. M. Patil, X. An, S. Li, X. Yue, X. Du, A. Yoshida, X. Hao, A. Abudula and G. Guan, Fabrication of three-dimensionally heterostructured rGO/$WO_3 \cdot 0.5$ H_2O@ Cu_2S electrodes for high-energy solid-state pouch-type asymmetric supercapacitor, *Chem. Eng. J.*, 2021, **403**, 126411.

82 T. Tahir, D. Alhashmialameer, S. Zulfiqar, A. M. Atia, M. F. Warsi, K. Chaudhary and H. M. El Refay, Wet chemical synthesis of Gd^{3+} doped vanadium Oxide/MXene based mesoporous hierarchical architectures as advanced supercapacitor material, *Ceram. Int.*, 2022, **48**, 24840–24849.

83 M. Mahmood, K. Chaudhary, M. Shahid, I. Shakir, P. O. Agboola and M. Aadil, Fabrication of MoO_3 Nanowires/MXene@ CC hybrid as highly conductive and flexible electrode for next-generation supercapacitors applications, *Ceram. Int.*, 2022, **48**, 19314–19323.

84 S. Rafiq, A. K. Alanazi, S. Bashir, A. Y. Elnaggar, G. A. Mersal, M. M. Ibrahim, S. Yousaf and K. Chaudhary, Optimization studies for nickel oxide/tin oxide (NiO/Xg SnO_2, X: 0.5, 1) based heterostructured composites to design high-performance supercapacitor electrode, *Phys. B*, 2022, **638**, 413931.

85 J. Gao, Y. Zhou, Z. Liu, H. Wang and Y. He, NiCo-Se nanoparticles encapsulated N-doped CNTs derived from prussian blue analogues for high performance supercapacitors, *Electrochim. Acta*, 2022, **411**, 140064.

86 F. Zheng, J. Wang, W. Liu, J. Zhou, H. Li, Y. Yu, P. Hu, W. Yan, Y. Liu and R. Li, Novel diverse-structured h-WO_3 nanoflake arrays as electrode materials for high performance supercapacitors, *Electrochim. Acta*, 2020, **334**, 135641.

87 F. Zheng, C. Xi, J. Xu, Y. Yu, W. Yang, P. Hu, Y. Li, Q. Zhen, S. Bashir and J. L. Liu, Facile preparation of WO_3 nano-fibers with super large aspect ratio for high performance supercapacitor, *J. Alloys Compd.*, 2019, **772**, 933–942.

88 V. Lokhande, T. Hussain, A. Shelke, A. Lokhande and T. Ji, Substitutional doping of WO_3 for Ca-ion based supercapacitor, *Chem. Eng. J.*, 2021, **424**, 130557.

89 P. Nagaraju, A. Alsalme, A. M. Alkathiri and R. Jayavel, Rapid synthesis of WO_3/graphene nanocomposite via in-situ microwave method with improved electrochemical properties, *J. Phys. Chem. Solids*, 2018, **120**, 250–260.

90 H. Peng, G. Ma, K. Sun, J. Mu, M. Luo and Z. Lei, High-performance aqueous asymmetric supercapacitor based on carbon nanofibers network and tungsten trioxide nanorod bundles electrodes, *Electrochim. Acta*, 2014, **147**, 54–61.

91 F. Nasreen, A. W. Anwar, A. Majeed, M. A. Ahmad, U. Ilyas and F. Ahmad, High performance and remarkable cyclic stability of a nanostructured RGO–CNT-WO_3 supercapacitor electrode, *RSC Adv.*, 2022, **12**, 11293–11302.

92 İ. İnce and S. Ersoy, Phase transformation of α-MnO_2 to β-MnO_2 induced by Cu doping: improved electrochemical performance for next generation supercapacitor, *Mater. Sci. Eng. B*, 2023, **295**, 116580.

93 N. M. Shinde, A. D. Jagadale, V. S. Kumbhar, T. R. Rana, J. Kim and C. D. Lokhande, Wet chemical synthesis of WO_3 thin films for supercapacitor application, *Korean J. Chem. Eng.*, 2015, **32**, 974–979.